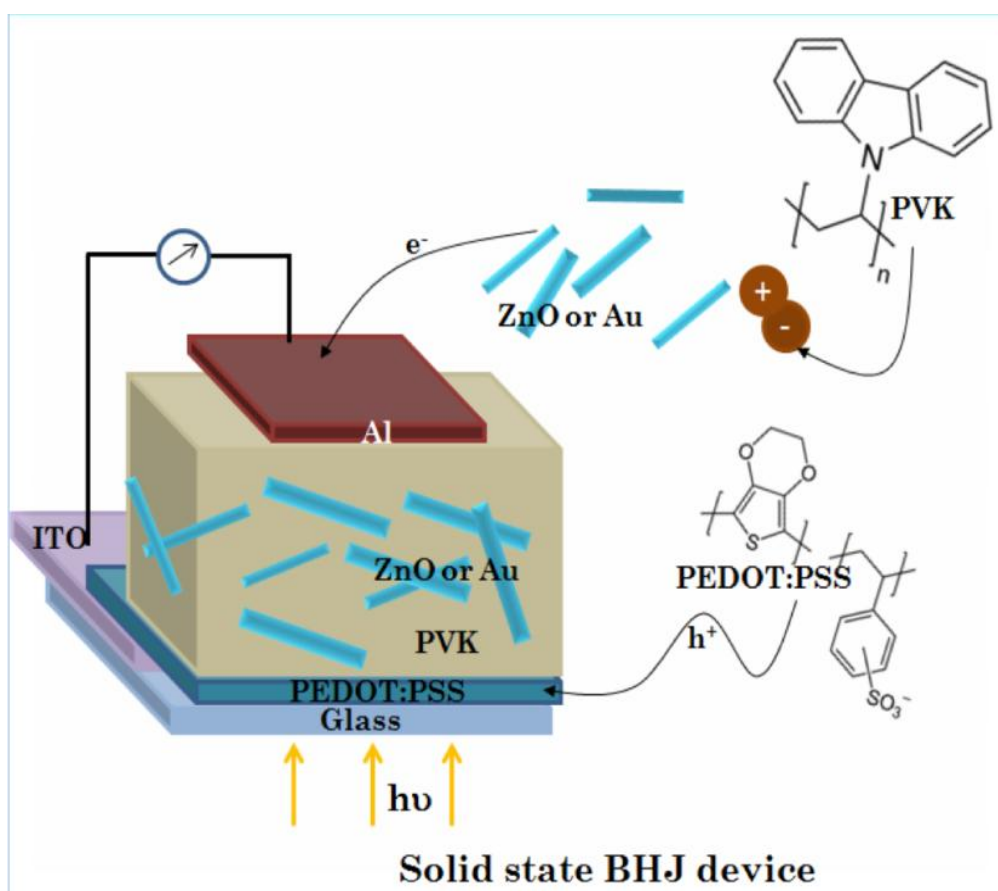# Chapter 2

Effect of aspect ratio of zinc oxide and gold nanorods on the photovoltaic performance of poly(9-vinylcarbazole) based bulk heterojunction solar cells

GRAPHICAL ABSTRACT

The high aspect ratio ZnO and Au nanorods are found to be effective in providing significant photovoltaic performance in PVK based solar cell

2.1 Introduction

For last few decades, hybrid BHJ solar cells based on polymer nanocomposite materials have attracted much attention in the solar energy research because of their high photo conversion efficiency (PCE) at low cost and easy fabrication procedure. Conducting polymers become more efficient as a hole transporting material in a photovoltaic device, if their band gap can be tuned to a suitable range by introducing nanofiller. Amongst various semiconducting polymers, carbazole-based polymer is very attractive because of its high thermal and photochemical stability, high charge carrier mobility, easy formation of relatively stable radical cations (holes), and easy substitution into the carbazole ring.[1] It is frequently used as a polymeric host material in photovoltaic devices.[2-4] Recently, much work is being investigated on exploring the photoconductivity of poly(9-vinylcarbazole) (PVK).[5-13] as well as its use as a polymeric host material in photovoltaics,[4, 14-18] although very low efficiency was observed.

Incorporation of n-type inorganic nanoparticles into a polymer matrix offers suitability of the hybrid material in solar cells due to a combined effect arising from processibility of the polymer in solution phase and greater electron mobility of the nanofiller. Semiconductor nanoparticles such as zinc oxide (ZnO) have attracted much interest in current research due to their environmental friendliness, large band gap, outstanding chemical and thermal stability and their specific properties like electrical

A part of this chapter is published:

S. Sharma, P. Gogoi, R. Bhargav, S.K. Dolui, A. Patra, *J. Polym. Mater.* 2015, 32 (2), 179-197.

S. Sharma, P.J. Bora, P. Gogoi, R. Boruah, K.J. Mohan, S.K. Dolui, *J. Mater. Sci. Mater. Electron.* 2015, 26, 5465-5474.

and optoelectronic properties.[19, 20] In an anisotropic ZnO nanoparticle such as nanorods, the optical absorption and other material properties can be tailored by changing their aspect ratios.[21] Among various synthesis methods, the hydrothermal method is the most energy efficient and economical method for the synthesis of anisotropic ZnO nanorods. The method is template-free, catalyst-free, environmentally friendly and less hazardous and it requires low process temperature and simple equipments and produces large area uniform nanocrystals.[22-24]

Another important class of photovoltaic architecture is the plasmonic BHJ devices, where a plasmonic metal nanoparticle is incorporated into the active layer. A polymer thin film solar cell is considered as one of the most cost effective and light-weight photovoltaic devices in recent times. Such a thin film has the ability to lower the probability of charge recombination, thus enhancing the internal quantum efficiency. But the optimum thickness of a thin film active layer is 100-200 nm which is not sufficient for efficient light absorption. This is the main challenging aspect of polymer thin film solar cells that results in low conversion efficiency. In this context, metal nanoparticles play a crucial role. They offer high light harvesting inside the active layer through increased light trapping due to the plasmonic effect of the nanoparticle. It causes enhancement of efficiency.[25] Anisotropic nanoparticles particularly nanorods show enhanced and size-dependent surface plasmon resonance (SPR) absorption which is tunable as a function of their aspect ratio. Gold (Au) metal nanorods show multiple absorption bands which can support both propagating and localized surface plasmons. They possess different resonance modes due to electron oscillation across and along the long axis of the nanorods. These are termed as transverse and longitudinal modes, respectively. The longitudinal mode is extremely sensitive to the aspect ratio of the nanorods.

This chapter describes the effect of individual nanoparticles on the performance of BHJ solar cells and is divided into two sections. The first section deals with the effect of different aspect ratio of ZnO nanorods on the photovoltaic performance of PVK based BHJ solar cells. The following section investigates the plasmonic effect of different aspect ratio of Au nanorods on PVK based devices. The effect of aspect ratio of the nanofiller is the central topic of discussion in both the sections.

Section A: Hybrid bulk heterojunction solar cells based on poly(9-vinylcarbazole)/zinc oxide (ZnO) nanocomposites: effect of aspect ratio of ZnO nanorods

2.2 Experimental

2.2.1 Reagents

Zinc acetate ($Zn(CH_3COO)_2$), sodium hydroxide (NaOH), cetyltrimethyl ammonium bromide (CTAB) and tetrahydrofuran (THF) were purchased from Merck India. 9-vinylcarbazole (NVK) was purchased from Sigma Aldrich. Benzoyl peroxide (BPO) was purchased from G. S. Chemical Testing Lab and Allied Industries, New Delhi. Poly (3,4-ethylenedioxythiopene) (PEDOT): poly (styrenesulfonate) (PSS), Phenyl-C_{61}-butyric acid methyl ester (PCBM) and indium tin oxide (ITO) coated glasses were purchased from Sigma Aldrich.

2.2.2 Synthesis of ZnO nanorods

A set of ZnO nanorods was synthesized by a simple hydrothermal route. In a typical synthesis, $Zn(CH_3COO)_2$ and CTAB were first dissolved in water in a 50 mL beaker and kept under continuous stirring. 0.6 M NaOH (aq) was added dropwise to this solution till the desired pH was achieved and continued stirring for 2 h. Then the solution was transferred into a teflon-sealed autoclave with capacity 50 mL and kept the autoclave into a hot-air oven at 100 ºC for 16 h. After the defined time period, the autoclave was allowed to cool. The white precipitates were filtered and washed thoroughly with distilled water and ethanol followed by drying at 50 ºC under vacuum. Molar ratio of $Zn(CH_3COO)_2$ and CTAB was fixed at 1:1.5. Only the concentration of NaOH was varied in the solution to keep the pH in the range 8.4-11.4 so as to study its effect on nanoparticle growth. The synthesized ZnO nanorods were denoted as Z-8.4, Z-9.4, Z-10.4 and Z-11.4 respectively, where the number denotes the pH of the medium.

2.2.3 Synthesis of poly(9-vinylcarbazole)/ZnO nanocomposites

PVK/ZnO nanocomposites were synthesized by an in-situ free radical chain polymerization of NVK in presence of ZnO nanofiller. In a three-necked round bottom flask, a mixture containing 0.005 mole of NVK (0.97 g), 1 wt% of BPO and 0.1 wt% of ZnO was dissolved in 5 mL THF. The solution was kept at a nitrogen atmosphere under stirring at 90 °C for 7 h. The remaining two necks of the round bottom flask were fitted with a condenser and a thermometer pocket. After the defined time period, the reactant mixture was cooled and precipitated in a mixed solvent of double distilled water and methanol. The precipitate was filtered and washed with ethanol followed by drying at 50 °C. The process was repeated to synthesize a set of nanocomposites by three different ZnO nanofiller prepared at different pH (Z-8.4, Z-10.4 and Z-11.4). The nanocomposites were designated as PZ-8.4, PZ-10.4 and PZ-11.4.

2.2.4 Fabrication of the device

A set of hybrid BHJ solar cell was fabricated in a standard squeeze structure of ITO/PEDOT:PSS/PVK/ZnO nanocomposite/Al and the complete fabrication procedure can be described as: prior to the fabrication, the ITO-coated glass substrates were cleaned by ultrasonication in detergent and de-ionized water followed by treatment in boiled acetone and isopropanol and finally dried. Then a thin layer of PEDOT:PSS (thickness 5 nm) was spin-coated onto the ITO film followed by annealing at 120 °C for 15-20 min. A 1 mL solution containing the nanocomposites (PZ-8.4, PZ-10.4 and PZ-11.4) in 1 mgmL^{-1} ratio was spin-coated with a rotation speed of 1800 rpm, onto the surface of PEDOT:PSS with a thickness of 50-80 nm. Finally, the aluminium cathode of thickness 100 nm was thermally evaporated in a vacuum coating unit at a pressure of $2x10^{-5}$ Pa. The cell has an active area of 0.04 cm^2. For comparison, a cell without ZnO was fabricated where PCBM replaced ZnO at a weight ratio of 1:1 with PVK.

2.3 Instruments and methods

2.3.1 Fourier transform infrared spectrometer (FT-IR)

FT-IR is a useful technique for the characterization of polymer and nanocomposites. It is primarily used for the detection of functional groups, but analysis of spectra in the

lower frequency finger print region can give an evidence of the effect of nanofillers on the electronic properties of the polymer backbone.

FT-IR analysis of synthesized nanocomposites was carried out in FT-IR Nicolet, (Impact 410) spectrophotometer (USA). Pellet, required for analysis, was prepared by a compression moulding under vacuum, by using a required amount of samples grounded and mixed properly with dried potassium bromide (KBr). The spectra were recorded in transmission mode in the range of 4000-400 cm^{-1} with a nominal resolution of 4 cm^{-1}.

2.3.2 X-ray diffractometer (XRD)

X-ray powder diffraction (XRD) is a rapid analytical technique primarily used for phase identification of a crystalline material and can provide information on unit cell dimensions. The analyzed material is finely ground, homogenized, and average bulk composition is determined.

Powder XRD data were collected on a Rigaku X-ray diffractometer (Miniflex, UK) under CuK$_{\alpha}$ (λ= 0.154nm) radiation at 30 kV and 15 mA with a scanning rate of 2° min^{-1} in a 2θ ranges from 10° to 80°.

2.3.3 Scanning electron microscopy (SEM)

The scanning electron microscope (SEM) is a type of electron microscope that images the sample surface by scanning it with a high energy beam of electrons (0.2-40 keV) in a raster scan pattern. The electrons interact with the atoms that make up the sample producing signals that contain information about the sample's surface topography, composition and other properties such as electrical conductivity.

SEM study was performed to investigate the surface morphology or microstructure of the sample. JSM-6390LV, JEOL, Japan was used for analysis at an accelerating voltage of 5-15 kV. The surface of the sample was Pt coated before observation.

2.3.4 Ultraviolet-visible spectroscopy (UV-visible)

Ultraviolet-visible (UV-visible) spectroscopy refers to absorption spectroscopy or

reflectance spectroscopy in the UV-visible spectral region. In this region of the electromagnetic spectrum, molecules containing π-electrons or non-bonding electrons can absorb the energy in the form of ultraviolet or visible light and undergo electronic transitions.

The UV-visible absorption spectra of the nanocomposites were obtained in a Shimadzu UV-2550 UV-visible spectrophotometer, taking water and THF as solvent and a wavelength ranges from 200 to 800 nm.

2.3.5 Photoluminescence spectroscopy (PL)

Photoluminescence spectroscopy is a non-contact, non-destructive method of probing the electronic structure of materials. In essence, light is directed onto a sample, where it is absorbed and where a process called photo-excitation can occur. The photo-excitation causes the material to jump to a higher electronic state, and will then release energy (photons) as it relaxes and returns to a lower energy level. The emission of light or luminescence through this process is photoluminescence, PL.

The PL analysis of the synthesized nanorods and nanocomposites was done using Perkin Elmer LS55 fluorescence spectrometer in a wavelength ranges from 300 to 800 nm and with an excitation wavelength of 310 nm.

2.3.6 Thermogravimetric analysis (TGA)

Thermogravimetric analysis (TGA) reveals the thermal characteristics of polymers and their nanocomposites including degradation temperature, absorbed moisture content the level of oligomer in polymer etc. It determines the weight loss with respect to temperature.

Thermogravimetric data was taken in a Shimazdu TGA 50 thermal analyzer at a heating rate of 10 °C min^{-1} and a temperature ranges from 25 °C to 600 °C under nitrogen (flow rate: 30 mL min^{-1}).

2.3.7 Cyclic voltammetry (CV) analysis

Cyclic Voltammetry (CV) is an electrochemical technique which measures the current

that develops in an electrochemical cell under conditions where voltage is in excess of that predicted by the Nernst equation. CV is performed by cycling the potential of a working electrode, and measuring the resulting current.

Electrochemical measurements were carried out in an electrochemical work-station (Model: Sycopel AEW2_10) equipped with three electrodes Ag/AgCl electrode (reference), Pt wire (counter) and glassy carbon electrode (working). Electrochemical characteristics of the polymer and the nanocomposite were investigated by CV scanning in 0.1 M lithium perchlorate ($LiClO_4$) supporting electrolyte solution in acetonitrile at a scan rate of 20 mVs^{-1}. The HOMO and LUMO energy levels as well as the energy gap (E_g^{ec}) can be calculated from the onset oxidation potentials (ϕ_{ox}) and the onset reduction potentials (ϕ_{red}) according to the following equations:

$$HOMO = -(\phi_{ox} + 4.71)\ eV \qquad \text{Eqn. 2.1}$$

$$LUMO = -(\phi_{red} + 4.71)\ eV \qquad \text{Eqn. 2.2}$$

$$E_g^{ec} = (\phi_{ox} - \phi_{red})\ eV \qquad \text{Eqn. 2.3}$$

2.3.8 Photovoltaic performance

Photovoltaic characterization of fabricated solar cells was carried out under simulated (AM1.5) solar illumination at 1 sun (100 mW/cm^2) in laboratory air. The device parameters are calculated using the following equations:

$$\text{Fill factor, FF} = \frac{J_{max} \cdot V_{max}}{J_{sc} \cdot V_{oc}} \qquad \text{Eqn. 2.4}$$

$$\text{Maximum power, } P_{max} = J_{max} \cdot V_{max} = J_{sc} \cdot V_{oc} \cdot FF \qquad \text{Eqn. 2.5}$$

$$\eta = \frac{P_{max}}{P_{in}} = \frac{J_{sc} \cdot V_{oc} \cdot FF}{P_{in}} \qquad \text{Eqn. 2.6}$$

where, J_{max} and V_{max} are the current density and voltage respectively at the maximum power point of the J-V curve. J_{sc} and V_{oc} are the short circuit current density and open circuit voltage respectively. FF is the fill factor. P_{in} is the intensity of the white light and η is PCE of the device.

2.4 Results and discussion

2.4.1 Growth mechanism of ZnO nanorods

In the hydrothermal method of synthesis of ZnO nanorods, the first intermediate product is $Zn(OH)_2$. During the reaction, it dissolves considerably to form Zn^{2+} and OH^-. The concentration of zinc and hydroxyl ions has a significant effect on nanoparticle formation as well as particle growth in a specified direction. We can define the solubility product (K_{sp}) as shown in Eqn. 2.7.

$$K_{sp} = [Zn^{2+}] \times [OH^-]^2 \qquad \text{Eqn. 2.7}$$

Once the solubility product exceeds a critical value, the ZnO nanocrystals are precipitated out. Because of the less solubility of ZnO compared to $Zn(OH)_2$, the first intermediate can effectively transform into ZnO nanocrystals during hydrothermal condition by the subsequent mechanism (Eqn. 2.8 & 2.9):

$$Zn(OH)_2 = Zn^{2+} + 2OH^- \qquad \text{Eqn. 2.8}$$
$$Zn^{2+} + 2OH^- = ZnO + H_2O \qquad \text{Eqn. 2.9}$$
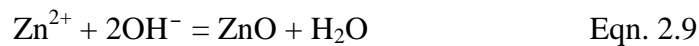
These newly formed ZnO nuclei take part in the growth of the nanorods as the structural blocks. The polar surfaces of ZnO nanoparticle ($Zn^{\delta+}-O^{\delta-}$) attract previously formed ZnO species and also the oppositely charged ions (OH^- or Zn^{2+}) towards them, which guide the one dimensional growth of ZnO nanocrystals resulting in the formation of nanorods.[21, 26] In the growth of ZnO nanocrystals, pH of the medium plays a vital role. Initially, concentrations of both the ions, Zn^{2+} and OH^- are remarkably higher that allow crystal growth in both lateral and longitudinal directions.[24] At the maximum pH, the excess concentration of OH^- dominates the concentration of Zn^{2+}. Therefore, nanoparticle growth is restricted to a particular direction and the nuclei grow by a diffusive mechanism into crystalline subunits thus forming high aspect ratio nanorods. The capping agent CTAB has a marked effect on modifying the morphology of the one-dimensional nanostructures. The function of CTAB micellar template is to control the particle growth along one particular dimension, thus stabilizing the nanorods. When CTAB is used, being a cationic surfactant, it ionizes completely in the growth solution, thus forming ions CTA^+ and B^-. The structure of CTA^+ cation is positively tetrahedral along with a lone

hydrophobic tail of cetyl group. It is being electrostatically attach with $Zn(OH)_4^{2-}$, thus forming a complexing agent. This complexing agent is adsorbed onto the surface of the ZnO nuclei and generates active sites for nanocrystal growth.[27] Moreover, being a surfactant CTAB may inhibit the lateral growth of the ZnO nanorods.[21]

2.4.2 Morphology (SEM-EDX)

Fig. 2.1a-b and 2.2a represent SEM micrographs of ZnO nanorods synthesized at different pH [Z-8.4, Z-10.4 and Z-11.4]. Micrographs depict the formation of ZnO nanorods with a diameter of ~155-188 nm. Both the concentrations of Zn^{2+} and OH^- are considerable upto a pH 10.4. Therefore, particle growth occurs in lateral and longitudinal directions in an equal proportion causing a gradual increase in diameter of the nanoparticles. Above pH 10.4, further increase in diameter of nanoparticle is not observed, but particle growth takes place significantly in the longitudinal direction.[24] Thus, excess concentration of OH^- dominates the concentration of Zn^{2+} and therefore, aspect ratio of nanorods increases significantly. For instance, the aspect ratio of nanorods at pH 8.4 is ~8, whereas it is ~20 at pH 11.4. EDX spectrum of ZnO
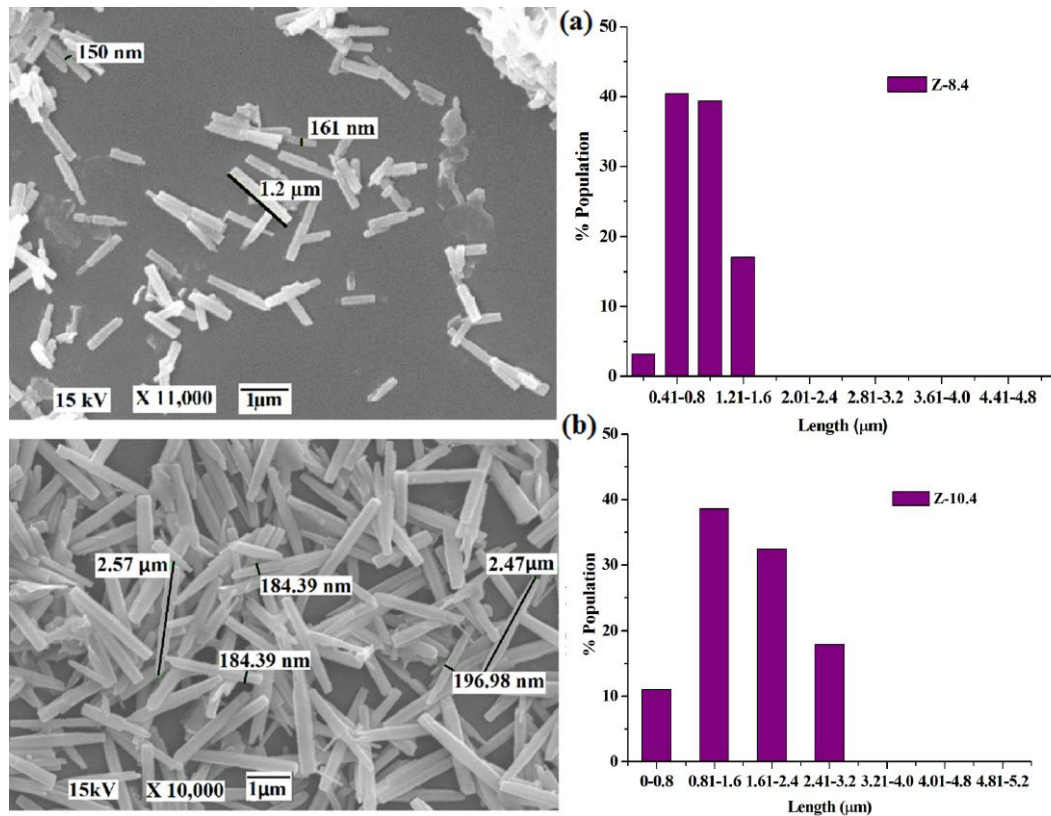
Fig. 2.1 SEM images of (a) Z-8.4 and (b) Z-10.4. *The number denotes the pH of the medium

nanorods [Fig. 2.2b] indicates the presence of equal proportion of both Zn and O in the nanostructure.

Morphological information about the surface of PVK/ZnO nanocomposite is obtained by SEM study. The SEM micrograph of the nanocomposite, PZ-11.4 [Fig. 2.2c] shows the homogeneous mixing of ZnO nanorods within the polymer matrix. The presence of ZnO nanorods in the nanocomposites is confirmed by EDX study [Fig. 2.2d].
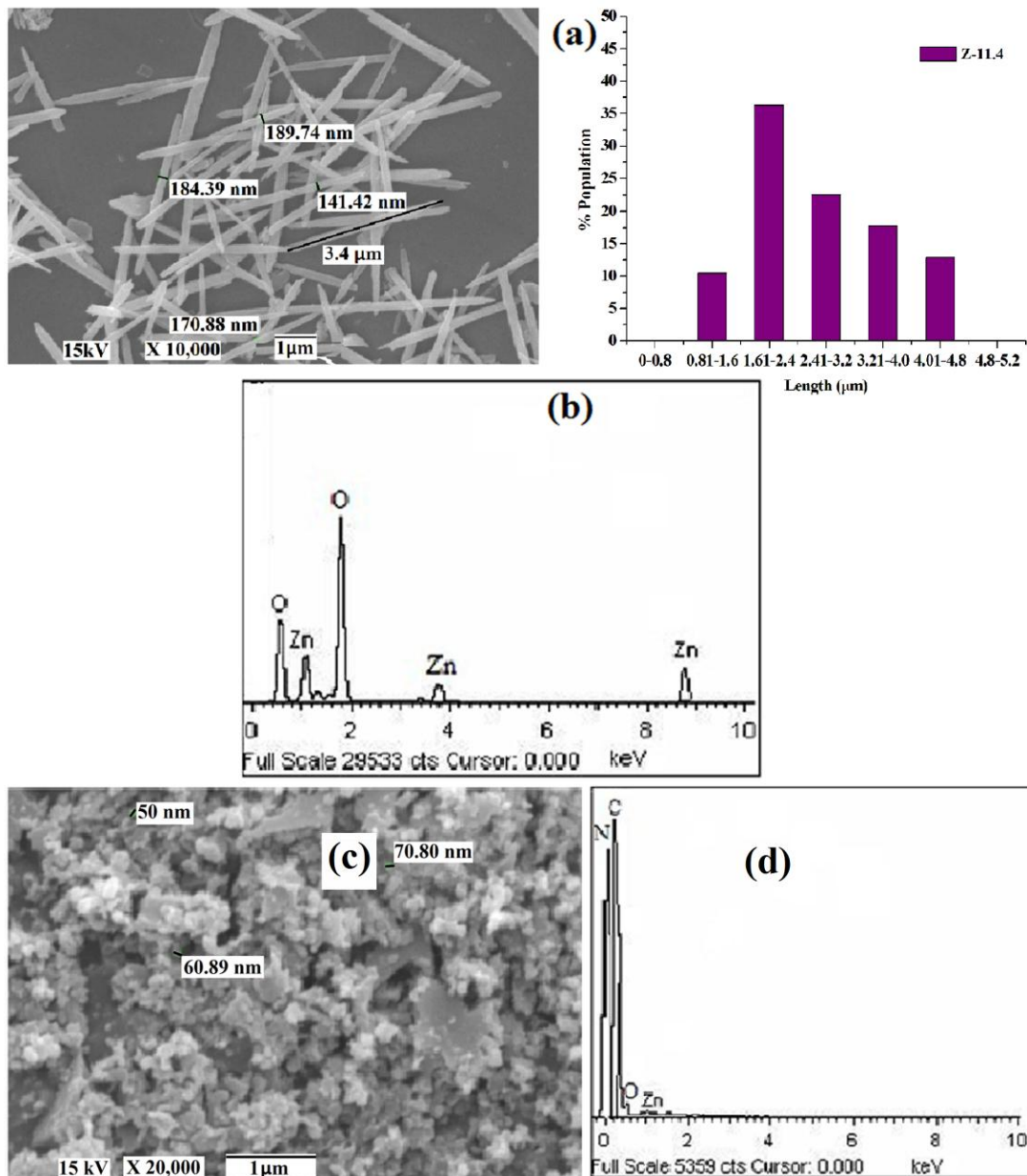
Fig. 2.2 (a) SEM image of Z-11.4, (b) EDX spectrum of Z-11.4, (c) SEM image and (d) EDX spectrum of PZ-11.4. *The number denotes the pH of the medium

2.4.3 Structural analysis (XRD, FT-IR)

Fig. 2.3 shows the XRD patterns of ZnO nanorods [Z-8.4, Z-10.4 and Z-11.4]. The diffraction peaks are well matched with hexagonal ZnO nanocrystals that agreed with the reported JCPDS (card no. 75-0576).[28] The intense diffraction peaks confirm the
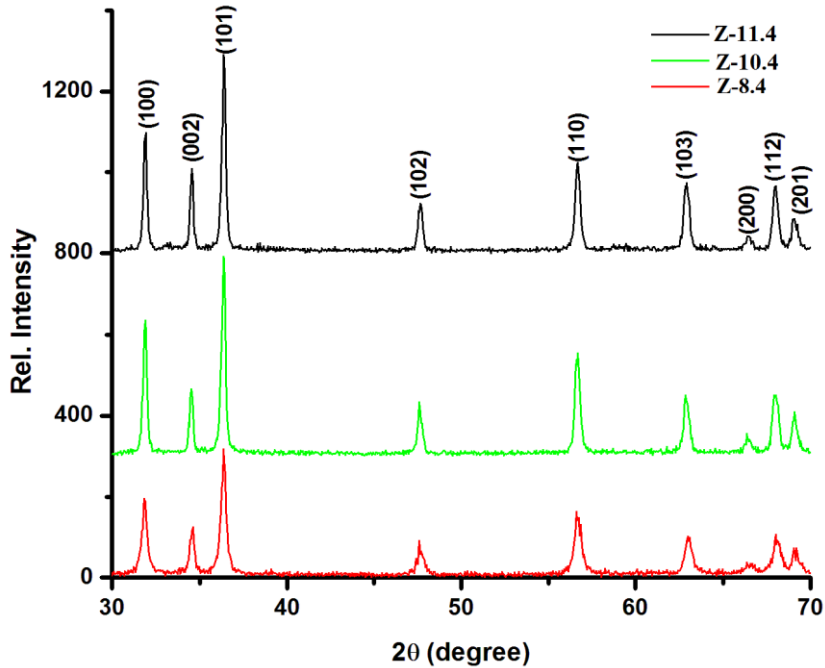

Fig. 2.3 XRD patterns of synthesized ZnO nanorods.
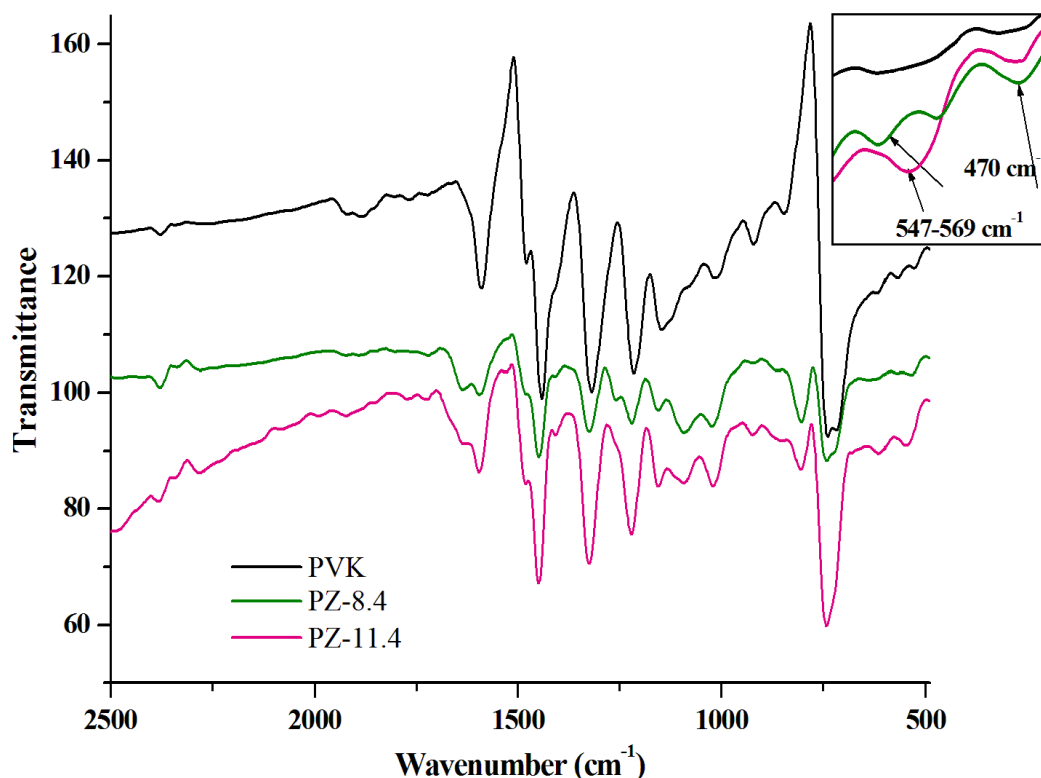*The number denotes the pH of the medium

formation of highly crystalline ZnO nanorods under the hydrothermal conditions. The diffraction peaks of all the samples reveal the formation of structurally uniform ZnO nanocrystals. To minimize the energy under the hydrothermal condition, the polar planes of ZnO grow faster than other planes along (001) direction, thus leading to the growth of nanorods, confirmed by XRD analysis.[21, 26] For the ZnO nanorods capped with CTAB, the (101) diffraction peak becomes stronger and narrower than the other peaks, which shows a preferential orientation along the c-axis.[26] The mean crystallite size of ZnO nanoparticles can be estimated using the standard Scherrer's equation into the diffraction intensity of (101) peak. The equation is:

$$D = 0.89 \ (\lambda/\beta \cos\theta) \qquad \text{Eqn. 2.10}$$

where, λ: wavelength (CuK$_\alpha$) = 0.154 nm, β: Full width at half-maxima (FWHM) of

ZnO (101) line, θ: the diffraction angle.

With increase in pH, the average crystallite size increases from 27 to 35 nm which may be due to more preferential growth of nanoparticle particularly in one specified direction [(001)] at higher pH of the medium.

Fig. 2.4 FT-IR spectra of PVK and the nanocomposites with two different aspect ratio ZnO nanorods. *The number denotes the pH of the medium. Inset shows the absorption band for Zn-O stretching

From FT-IR analysis [Fig. 2.4], various characteristic peaks are observed for PVK. The stretching frequency at 730 cm^{-1} is attributed to the deformation of substituted aromatic ring. Whereas, the out-of-plane deformation band, related to vinylidene group, appears at 1011-1150 cm^{-1}. The bands at 1217 and 1320 cm^{-1} are due to the stretching C-N bond of carbazole moiety and bands at 1594 cm^{-1} and 1444 cm^{-1} are due to C=C aromatic stretching. Stretching frequencies at 2935 cm^{-1} and 3043 cm^{-1} are due to aliphatic C-H and aromatic C-H stretching respectively.[29] The disappearance of the peak at 1600-1680 cm^{-1} is the indication of an effective polymerization at the vinyl group. These characteristic peaks are also observed in all PVK/ZnO nanocomposites. In the nanocomposites the shifting in peak positions of the bands associated with C=C

and C-N bonds towards higher wavenumber strongly suggests withdraw of electrons by ZnO from the anti-bonding orbitals of the respective bonds [Fig. 2.4]. Again, in the finger print region two absorption bands are found at 470 cm^{-1} and 547-569 cm^{-1} in the nanocomposites [Fig. 2.4 inset] which can be attributed to the Zn-O stretching.[30]

2.4.4 Optical study (UV-visible, PL)

From the UV-visible spectra [Fig. 2.5a] of ZnO nanorods (from Z-8.4 to Z-11.4), strong absorption peaks are observed at 379-400 nm due to the formation of wide band gap ZnO nanorods.[21] With increase in pH from 8.4 to 11.4, the absorption shows a bathochromic shift remarkably upto 21 nm which indicates the increase of size of the nanoparticles with increase in pH. The optical band gap of nanoparticles decreases with increase in nanoparticle size as a consequence of which absorbance shows a red-shift. With increase in pH, OH$^-$ concentration dominates the Zn^{2+} concentration, which restricts the lateral growth of particle thus promoting the nanoparticle growth significantly along longitudinal direction.[24] Therefore, the length of the nanoparticle significantly increases that enhances the aspect ratio to a large extent. Consequently, absorption shows a red-shift at higher pH.

The possible mechanism behind nanorods nucleation is also related to specific surface energies intrinsic in different planes of ZnO nanocrystals. It is known that the specific surface energies held by the planes of a particular crystal determine its crystal morphology. The variation in surface energies causes some planes of the crystal to absorb preferentially OH$^-$ ions prior to the binding of growth units into a crystal lattice. This possibly impedes the movement of Zn^{2+} in the grown nucleus in one particular direction. In this condition, OH$^-$ ions act as a nucleation center where free Zn^{2+} ions react with OH$^-$ in a direction with less OH$^-$ concentration, nucleating into ZnO nanorods.[31] Thus, it can be concluded that OH$^-$ concentration is a dominant factor for ZnO nanocrystal growth. These results are supported by the XRD data [Fig. 2.3].

The ultraviolet-visible absorption spectra of PVK/ZnO nanocomposites are recorded to study the effect of nanorods on the optical property of PVK. PVK shows intensive absorption peaks [Fig. 2.5b] at 245 and 266 nm which are attributed to $\pi \rightarrow \pi^*$ electronic transition of the carbazole ring.[32] Significant changes are noticed in the
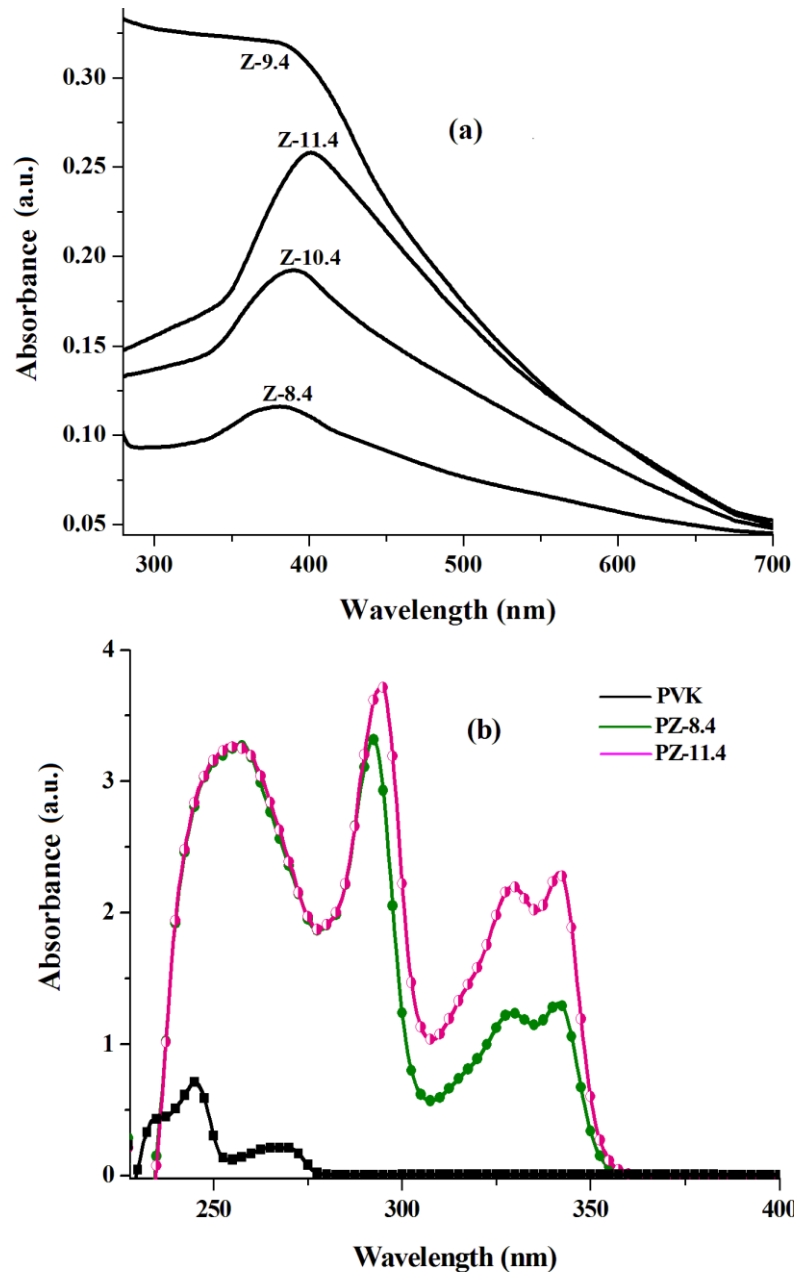
Fig. 2.5 UV-visible spectra of (a) ZnO nanorods and (b) polymer and the nanocomposites with two different aspect ratio of ZnO nanorods. [*]The number denotes the pH of the medium.

optical spectra of nanocomposites [Fig. 2.5b]. Incorporation of ZnO nanorods within the PVK matrix shows a shifting of the peaks (up to 28 nm) towards higher wavelength, i.e., bathochromic shift is observed in the nanocomposites. It clearly indicates that the incorporation of ZnO nanorods within the PVK matrix modifies the electronic structure of the polymer resulting in reduced optical band gap of the polymer [Table 2.1]. ZnO nanorods can form localized electronic states between

HOMO and LUMO levels of PVK thus altering the electronic states of the polymer. This leads to the observed change in the optical band gap.[33] With increase in aspect ratio of the nanorods, more number of localized electronic states are formed thus leading to further decrease in optical band gap. Moreover, the appearance of strong absorption peaks in the region 329-340 nm is due to the presence of ZnO nanorods into the polymer matrix.[21] Thus, the overall absorbance of the nanocomposite shows a significant red shift (up to 80 nm) with a remarkable hyperchromicity due to a combined effect of both polymer and nanorods. High aspect ratio nanorods have more contribution towards enhancement of optical absorbance, which may be due to the enhancement of ZnO amount in the nanocomposite that enhances the optical absorbance.[34]

Table 2.1 Optical and electrochemical properties of the nanocomposites

Sample particulate	E_g^{op} (eV)	E_g^{ec} (eV)
PVK (0)	4.5	1.89
PZ-8.4 (8)	3.54	1.30
PZ-11.4 (20)	3.50	1.01

*The number denotes the pH of the medium and that in the bracket denotes the aspect ratio of ZnO nanorods in the nanocomposites

Fig. 2.6a-c illustrate the PL spectra (λ_{ex} = 310 nm) and their corresponding de-convoluted spectra of ZnO nanorods [Z-8.4 and Z-11.4]. The PL spectrum shows a wide emission in the visible region ranging from 350-550 nm resulting from the radiative emission due to various defect states related to ZnO, such as zinc and oxygen vacancies and interstitials. The broad band is composed of four types of characteristic emission peaks of ZnO nanorods. Peaks at around 420, 393, 490 and 455 nm are due to neutral zinc interstitial (Zn_i), neutral zinc vacancy (V_{Zn}^0), singly ionized oxygen vacancy (V_O^+) and singly ionized zinc interstitial (Zn_i^+) respectively.[19] Table 2.2 summarizes the effect of pH change on the emission peak for V_{Zn}^0 and Zn_i^+. It is observed that, as the pH of the medium increases, the emission peak for V_{zn}^0 and Zn_i^+ dominate over Zn_i. V_o^+ and Zn_i defects in ZnO nanorod represent donors whereas V_{Zn}^0 and Zn_i^+ represent acceptors.[19] Therefore, the dominance of Zn_i^+ and V_{Zn}^0 peaks imparts a good n-type characteristic to the ZnO nanorod.
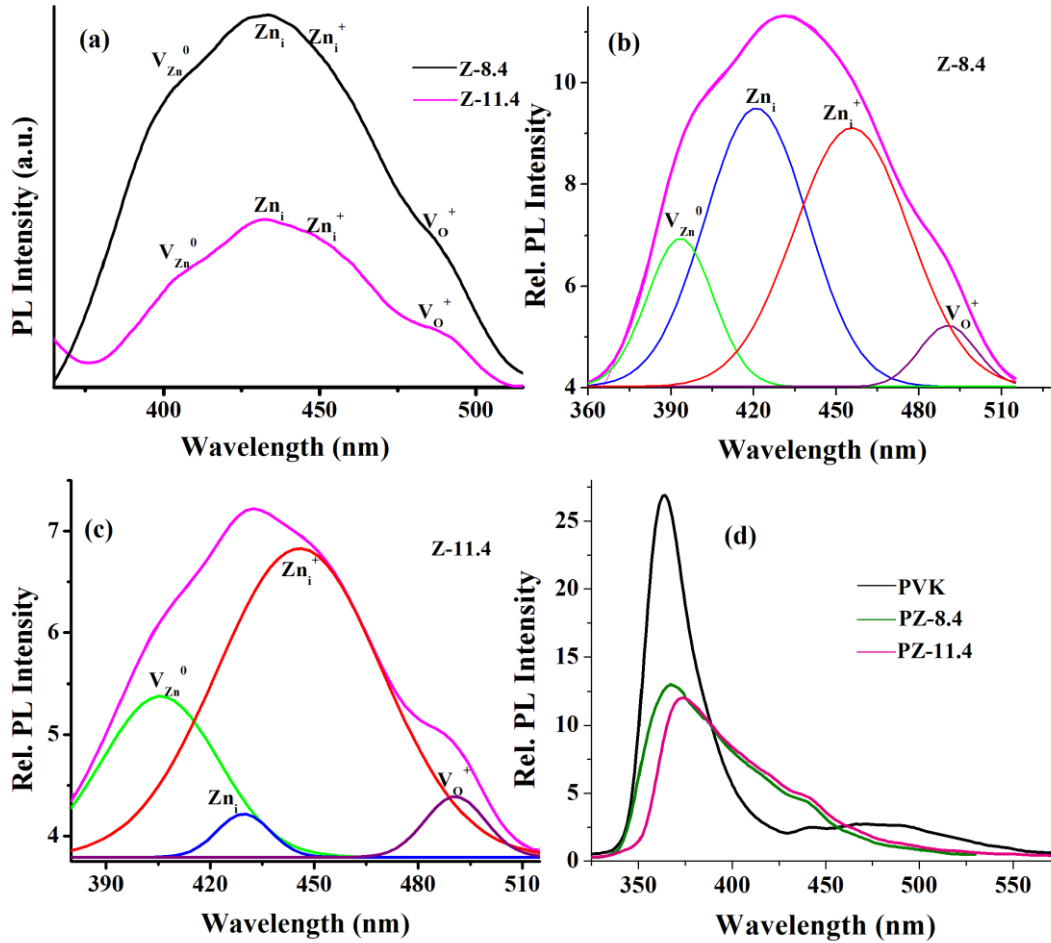
Fig. 2.6 (a) PL spectra of ZnO nanorods, (b) de-convoluted spectrum of Z-8.4, (c) de-convoluted spectrum of Z-11.4 and (d) PL spectra of the polymer and nanocomposites. *The number denotes the pH of the medium.

Table 2.2 n-type and p-type characteristics in synthesized ZnO nanorods

Sample particulate	Zn_i/Zn_i^+	Zn_i/V_{Zn}^0	Zn_i^+/V_O^+
Z-8.4	1.08	1.87	4.23
Z-11.4	0.14	0.27	5.067

Before investigating the effect of ZnO nanorods on the device performance of the solar cells, it is needful to see how this affects charge formation. For this purpose, we study the PL property of the nanocomposites [Fig. 2.6d]. Both PVK and PVK/ZnO nanocomposites were excited at 230 nm and corresponding emission spectra were recorded. Two distinct fluorescence peaks are observed for PVK at 364 nm and 466 nm. The peaks are originated from the low energy intra-chain excimer recombination of the carbazole groups.[35] A remarkable change is noticed in emission spectra of

PVK/ZnO nanocomposites. The intensity of both the peaks of PVK remarkably reduces to 52-56%; to be precise, a PL quenching is observed which arises from the electron transfer from PVK to ZnO nanorods.[2] From these results, we can say that a maximum of 56% of the absorbed photons leads to exciton dissociation followed by charge separation at the PVK:ZnO interface.

2.4.5 Thermogravimetric analysis (TGA)

One of the most important properties in polymer nanocomposites is their thermal property. The thermal stability of the PVK/ZnO nanocomposites are investigated by using TGA and the weight loss traces recorded in the temperature range 25-600 °C as shown in Fig. 2.7. The TGA values of PVK/ZnO nanocomposites and their pristine polymer are summarized in Table 2.3. An enhanced thermal stability can be seen for PZ-8.4 and PZ-11.4. For example, the major degradation rate is remarkably shifted to 377° and 390 °C for the nanocomposites PZ-8.4 and PZ-11.4 respectively, which was at 350 °C for their pristine polymer [Table 2.3]. The possible mechanism behind the thermal degradation is the formation of free-radicals at the weak chains followed by radical transfer from chain-to-chain via inter-chain reactions. The enhancement of thermal stability in the nanocomposites can be illustrated in terms of the reduced mobility of the polymer chain. The reduced chain mobility suppresses the chain transfer reactions as a consequence of which the degradation process is delayed and decomposition takes place at comparatively high temperature.[36] The strong interaction between ZnO nanorods and polymer matrix is said to be solely responsible for this behaviour. The incorporation of ZnO within the polymer matrix impedes the mass transport of the volatile products generated during degradation process that offers high thermal stability in the nanocomposite.[37] From Table 2.3 it is observed that PZ-11.4 has more thermal stability than PZ-8.4. This may be attributed to the formation of more effective mass transport barrier to the volatile products, thereby increasing the overall stability.[38, 39]

Similar results were obtained with the nanocomposites mentioned earlier.[37, 40] The nanocomposites also show higher char content at 600 °C [Table 2.3]. The nanocomposites show char content of about 4 and 9 % for PZ-8.4 and PZ-11.4, while the pristine polymer shows about 1%. Thus, we can say that the incorporation of the

ZnO nanorods resulted in significantly improved thermal stability of the nanocomposites.
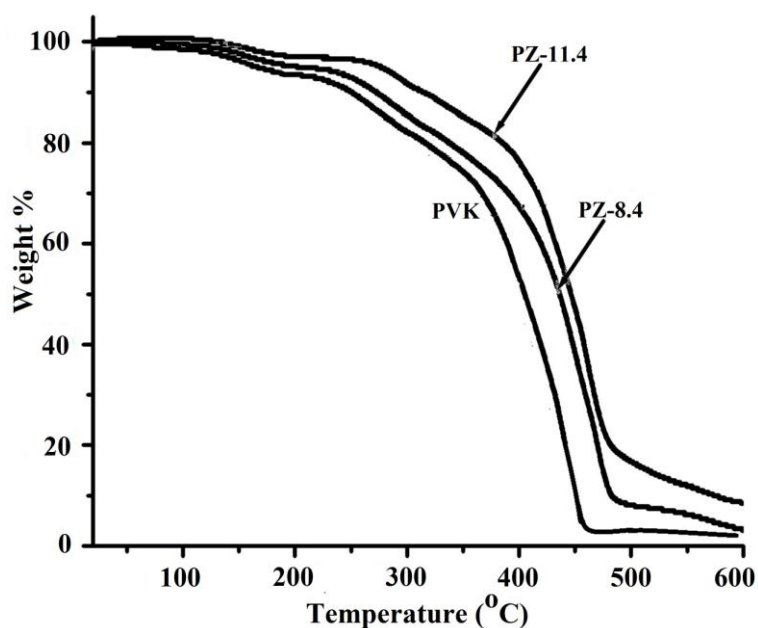
Fig. 2.7 Thermogravimetric curves of polymer and nanocomposites with two different aspect ratio of ZnO nanorods. *The number denotes the pH of the medium.

Table 2.3 The TGA values of polymer and nanocomposites

Sample particulate	Major degradation temperature (°C)	Deg. temperature for weight loss (°C)			Char content (%)
		2%	20%	50%	
PVK	350	127	322	422	1
PZ-8.4	377	144	337	437	4
PZ-11.4	390	172	385	447	9

2.4.6 Electrochemical (CV) analysis

The cyclic voltammograms (CV) of PVK and PVK/ZnO nanocomposites are presented in Fig. 2.8 and the values are summarized in Table 2.1. It is observed that the electrochemical band gap (E_g^{ec}) of PVK decreases linearly with increasing the ZnO nanorod aspect ratio in the nanocomposites. For instance, E_g^{ec} decreased by 0.88 eV for ZnO nanorods of aspect ratio 20, whereas the same decreased by only 0.59 eV for ZnO nanorods of aspect ratio 8. It can be attributed to the formation of large number of

localized electronic states in between HOMO and LUMO levels of PVK which alters the electronic states of the polymer. This leads to the decrease in band gap of the polymer.[33] Higher the aspect ratio of ZnO nanorods, more pronounced is the effect. Electrochemical properties of the nanocomposites can be correlated with their optical properties. Same trend is observed in case of optical band gap energy of the nanocomposites [Table 2.1].
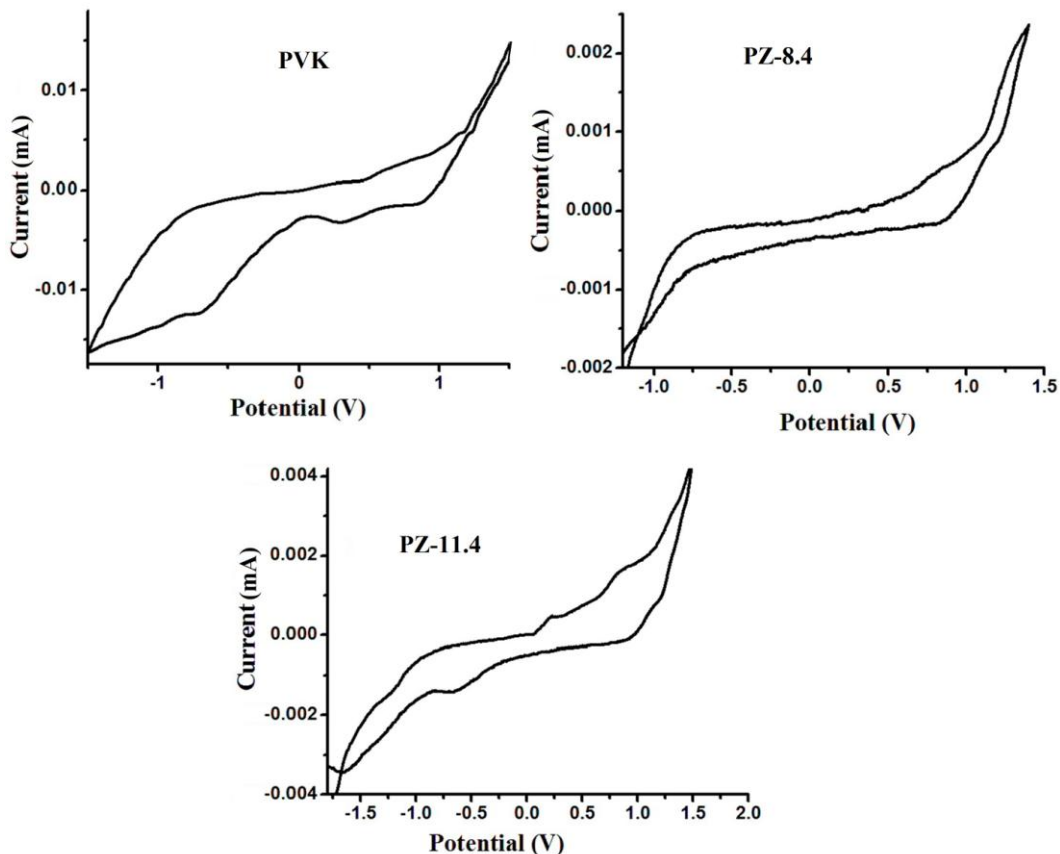

Fig. 2.8 Cyclic voltammetry curves of polymer and nanocomposites with two different aspect ratios of ZnO nanorods. *The number denotes the pH of the medium.

2.4.7 Study of photovoltaic performance

Photovoltaic properties of synthesized PVK/ZnO nanocomposites are studied by fabricating solar cells of the simple architecture, ITO/PEDOT:PSS/PVK/ZnO nanocomposite/Al. Here, PVK serves as the donor and ZnO nanorods act as the electron acceptor. PVK absorbs light and produces electron-hole pair bound by strong coulombic interaction, called exciton. This exciton has a very little mobility and it has the tendency to easily recombine. Therefore, to achieve photocurrent through electron transfer, exciton dissociation has to occur. For this purpose we use an electron

acceptor, ZnO that causes significant exciton separation followed by dissociation at the interface of hybrid BHJ under the effect of the internal field. Finally, charge collection occurs at the two electrodes (Al and ITO) causing a voltage difference between the electrodes. J-V graphs of the fabricated hybrid BHJ solar cells, obtained under AM-1.5 illumination at 100 mW/cm^2 are shown in Fig. 2.9a and photovoltaic parameters, obtained thereafter are mentioned in Table 2.4.
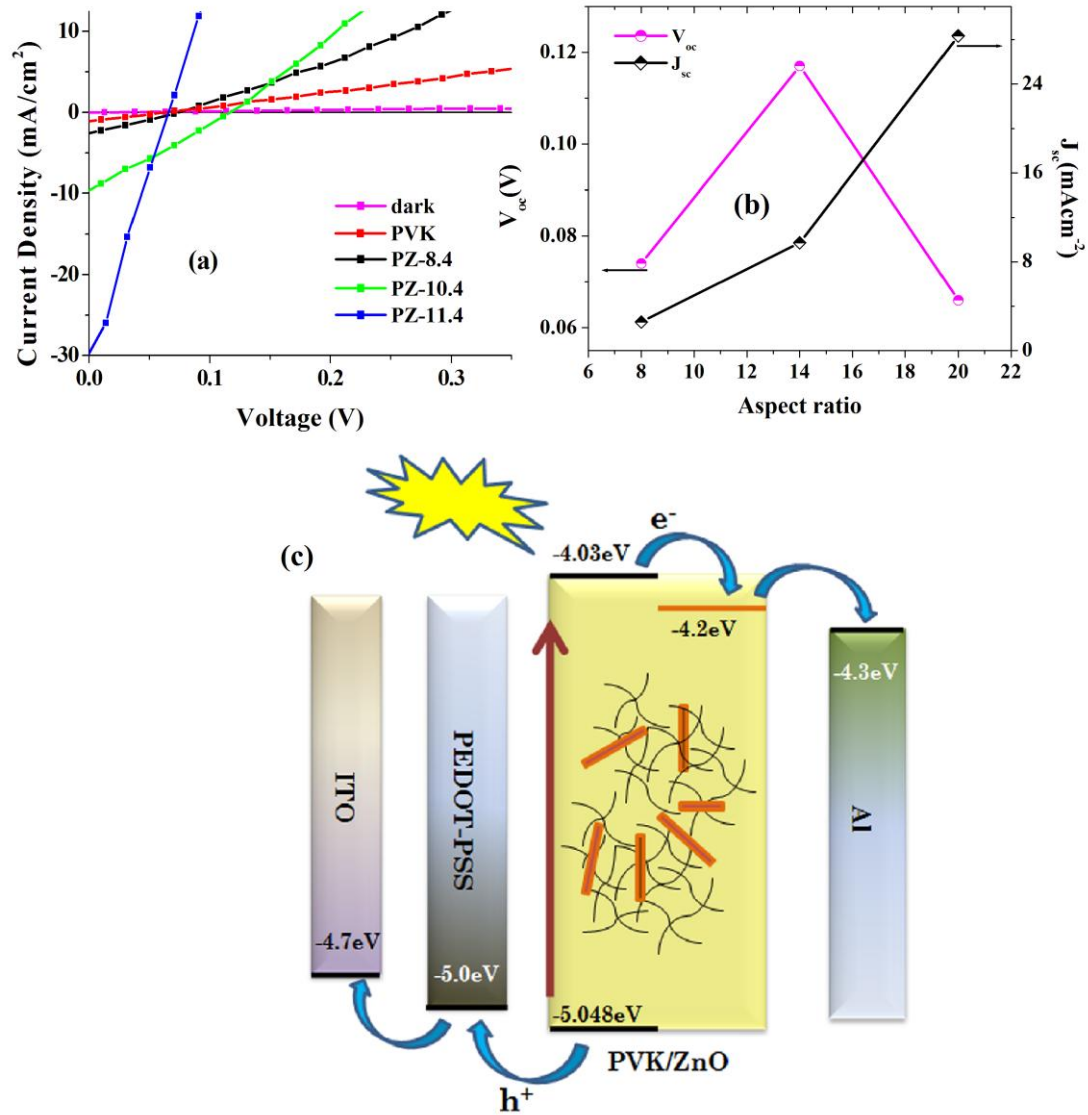
Fig. 2.9 (a) J-V curves of the fabricated devices under illumination, (b) shows how V_{oc} and J_{sc} changes with aspect ratio; (c) Schematic energy-level diagram for the devices

ZnO nanorod plays a significant part in the device performance of the solar cells. ZnO acts as a better electron acceptor than PCBM, as the LUMO levels of the polymer and ZnO are closer for efficient electron transfer formed during exciton dissociation that

offers better PCE of 0.05-0.44% [Fig. 2.9c]. The aspect ratio of nanorods has a significant impact on efficiency. V_{oc} increases initially with increasing the aspect ratio

Table 2.4 Photovoltaic characteristics of the devices

Sample code	V_{oc} (V)	J_{sc} (mA/cm^2)	FF	PCE, η (%)
PVK (0)	0.05	1.08	0.31	0.02
PZ-8.4 (8)	0.07	2.60	0.26	0.05
PZ-10.4 (14)	0.12	9.73	0.26	0.30
PZ-11.4 (20)	0.07	28.35	0.24	0.44

which may be due to increased shunt resistance in the device [Fig. 2.9b]. After a certain aspect ratio (14), shunt formation occurs, i.e., the current diverted through the shunt resistor that causes decrease in V_{oc} as well.[34] With increase in the aspect ratio, J_{sc} increases which arises from the increased charge formation, deduced from PL quenching. Another explanation might be the formation of more percolation pathways with increasing the aspect ratio of nanorods that facilitates the transport of electrons and photocurrent as well.[34] Thus, PCE increases with increasing the aspect ratio of nanorods. The device with ZnO nanorods (aspect ratio 8) shows PCE of 0.05%, while the device with nanorods (aspect ratio 20) shows a significantly higher value of 0.44%.

2.5 Conclusion

By compiling the results, we have come to the following conclusion:

♦ ZnO nanorods of various aspect ratios were synthesized successfully and incorporated into the PVK polymer matrix.

♦ Incorporation of high aspect ratio ZnO nanorods imparts significant improvement in thermal stability of the nanocomposites.

♦ The addition of nanorods into PVK matrix reduces the electrochemical and optical band gap of the polymer significantly by 0.88-1.0 eV as can be seen from the CV and UV-visible spectroscopy measurements.

♦ Effective exciton dissociation and electron transfer from PVK to ZnO occurs through PL quenching which offers the suitability of the nanocomposite in donor acceptor hybrid BHJ devices.

♦ The PCE of a hybrid BHJ solar cell can be increased to 0.44% with the incorporation of high aspect ratio ZnO nanorods into the active layer. With increasing the aspect ratio, J_{sc} of the devices increases due to the formation of large number of charges and more percolation pathways that allow the transport of electrons.

Section B: Plasmonic bulk heterojunction photovoltaic devices based on poly (9-vinylcarbazole)/gold (Au) nanocomposites: effect of aspect ratio of Au nanorods

2.6 Experimental

2.6.1 Reagents

Sodium borohydride ($NaBH_4$), CTAB, ascorbic acid, tetrahydrofuran (THF) and chlorobenzene were purchased from Merck India. Silver nitrate ($AgNO_3$) was purchased from Rankem. Chloroauric acid ($HAuCl_4$), NVK, poly(3,4-ethylenedioxythiopene): poly (styrenesulfonate) (PEDOT:PSS), phenyl-C_{61}-butyric acid methyl ester (PCBM) and indium tin oxide (ITO) coated glasses were purchased from Sigma Aldrich. Benzoyl peroxide (BPO) was purchased from G. S. Chemical Testing Lab and Allied Industries, New Delhi. All the chemicals are used as received.

2.6.2 Preparation of seed solution

To study the effect of size and shape of Au nanorods on the device performance, four anisotropic Au nanorod samples with different aspect ratio were synthesized using a seeded growth method, whereby the concentrations of growth solution were varied to control the shape as well as aspect ratio. Au nanorods were synthesized by the method described by Nikoobakht and El-Sayed.[41] In this method CTAB solution (5 mL, 0.2 M) was mixed with 5 mL of 0.001292 M $HAuCl_4$. To the stirred solution, 0.60 mL of ice cold 0.01 M $NaBH_4$ was added, which resulted in the formation of a brownish yellow solution. The vigorous stirring of the seed solution was continued for ~2 min. If we use tri-sodium citrate as the capping agent instead of CTAB, the citrate-capped seeds may form preferably star shaped nanocrystals.[41] Therefore, to avoid this problem we used CTAB instead.

2.6.3 Growth of nanorods

CTAB (5 mL, 0.20 M) was added to 0.25, 0.15, 0.05 mL of 0.0040 M $AgNO_3$ solution at room temperature. To this solution, 5 mL of 0.0010 M $HAuCl_4$ was added and after gentle mixing of the solution 70 µL of 0.0788 M ascorbic acid was added. Ascorbic

acid as a mild reducing agent changes the growth solution from dark yellow to colourless. The concentrations of Ag^+ ion in the growth solution were 9.8 x 10^{-5}, 5.9 x 10^{-5} and 2.03 x 10^{-5} M for 0.25, 0.15 and 0.05 mL of 0.0040 M $AgNO_3$ solution respectively. The final step was the addition of 12 μL of the seed solution to the growth solution at room temperature. The color of the solution has gradually changed within 10-20 min. For longer nanorods the color change takes place more slowly. The temperature of the growth medium was kept constant at room temperature in all the experiments. In all the nanoparticle dispersion, some amount of particles cannot grow during the reaction. Therefore, Au nanorods were centrifuged for several times and then re-dispersed in water to remove spherical nanoparticles and also the reactants as well as stabilizing agents. The overall reaction scheme of the seeded growth method is shown in (Scheme 2.1).
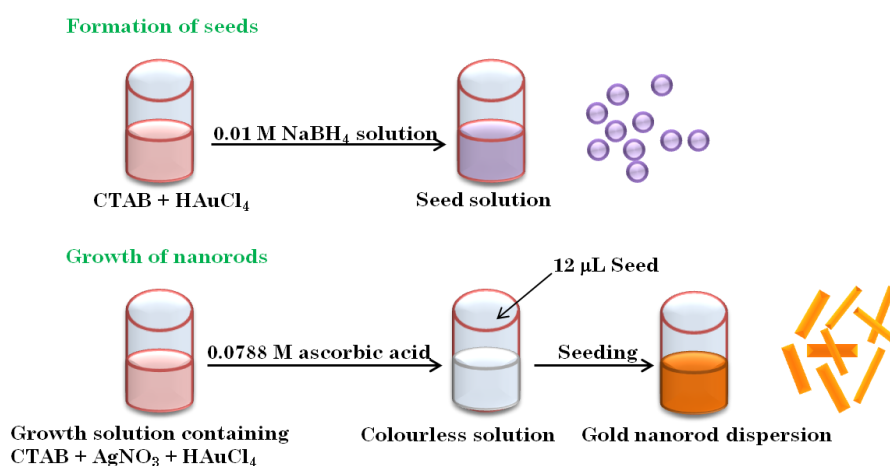
Scheme 2.1 Schematic representation of the seeded growth method

2.6.4 Synthesis of poly(9-vinylcarbazole)/Au nanocomposite

PVK and PVK/Au nanocomposites were synthesized by a solution polymerization of NVK. First 0.005 mol NVK (0.965 g) was dissolved in 5 mL THF and kept the solution into a three-necked round bottom flask fitted with a thermometer and a condenser where the polymerization was carried out at temperature range 85-95 °C. The flask was magnetically stirred and during stirring 1 % initiator, BPO and 0.25 % Au nano dispersion was added into the solution. Polymerization was carried out for 7 h. After polymerization the flask was allowed to cool to room temperature and by precipitation and filtration method finally the products were collected. The process

was repeated for a set of Au nano dispersion prepared at different Ag^+ ion concentration (9.8 x 10^{-5}, 5.9 x 10^{-5} and 2.03 x 10^{-5} M).

2.6.5 Fabrication of the photovoltaic device

Photovoltaic devices were fabricated in a typical sandwich structure of ITO/PEDOT:PSS/PVK/Au nanocomposite:PCBM/Al and the complete fabrication procedure can be described as: the ITO-coated glass substrates were cleaned by ultrasonic treatment in de-ionized water, acetone, detergent, and isopropyl alcohol sequentially under the treatment of ultrasonication and dried. Then a thin layer of PEDOT:PSS (thickness 10 nm) was spin coated onto the ITO coating followed by thermal treatment at 80-100 °C for 2 h. A total of 0.25 mL solution containing a homogeneous mixture of 1:1 nanocomposite and PCBM, dissolved in chlorobenzene was prepared under ultrasonication and spin coated at a rotation speed of 1200 rpm, onto the surface of PEDOT:PSS with a thickness of 50-80 nm. In all the nanocomposite samples, concentration of Au nanorods was kept constant at a 0.25 % of the monomer. Finally, aluminium cathode was thermally evaporated in a vacuum coating unit at a pressure of 4 x 10^{-5} Pa. The active area of the device was 1 cm^2.

2.7 Instruments and methods

2.7.1 Transmission electron microscope (TEM)

Transmission electron microscopy (TEM) is a microscopy technique whereby a beam of electrons is transmitted through an ultra thin specimen, interacting with the specimen as it passes through. An image is formed from the interaction of the electrons transmitted through the specimen; the image is magnified and focused onto an imaging device. TEM is capable of imaging at a significantly higher resolution than light microscopes, owing to the small de Broglie wavelength of electrons. This enables to examine fine detail of even as small as a single column of atoms, which is tens of thousands times smaller than the smallest resolvable object in a light microscope.

The morphology as well as size of the Au nanorods is investigated by transmission electron microscope (JEM 2100) with an acceleration voltage of 100-300 kV.

2.7.2 Scanning electron microscopy (SEM)

Surface morphology of the samples was investigated by SEM (Model:JSM-6390LV, JEOL, Japan) at an accelerating voltage of 5-15 kV. The surface of the sample was Pt coated before observation.

2.7.3 Fourier transform infrared spectrometer (FT-IR)

FT-IR spectra of the samples were recorded in FT-IR Nicolet, (Impact 410) spectrophotometer (USA). Pellet, required for analysis, was prepared by a compression moulding under vacuum, by using a required amount of samples grounded and mixed properly with dried KBr. The spectra were recorded in transmission mode in the range of 4000-400 cm^{-1} with a nominal resolution of 4 cm^{-1}.

2.7.4 Ultraviolet-visible spectroscopy (UV-visible)

The UV-vis spectra of the samples were recorded in a ultraviolet-visible spectrophotometer (Model: Shimadzu UV-2550) taking water and THF as solvent and a wavelength ranges from 200 to 800 nm.

2.7.5 Photoluminescence spectroscopy (PL)

The PL spectra of the Au nanorods were recorded by using a fluorescence spectrometer (Model: Perkin Elmer LS55) in a wavelength ranges from 300 to 800 nm and with an excitation wavelength of 510 nm.

2.7.6 Cyclic voltammetry (CV) analysis

Electrochemical property of the synthesized nanocomposites was investigated by using an electrochemical work-station (Model: Sycopel AEW2_10) equipped with three electrodes Ag/AgCl electrode (reference), Pt wire (counter) and glassy carbon electrode (working). CV analysis was performed by scanning the sample in 0.1 M lithium perchlorate ($LiClO_4$) supporting electrolyte solution in acetonitrile at a scan rate of 20 mVs^{-1}. The HOMO and LUMO energy levels as well as the energy gap (E_g^{ec}) can be calculated from the onset oxidation potentials (ϕ_{ox}) and the onset reduction potentials (ϕ_{red}) by using the equations [Eqn. 2.1-2.3].
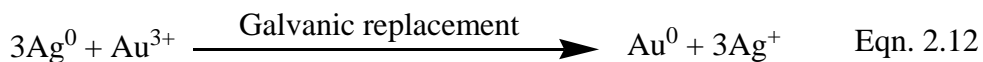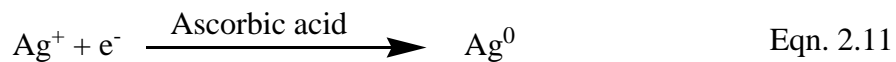
2.7.7 Photovoltaic characteristic of the photovoltaic devices

Photovoltaic characterization of the fabricated devices was carried out under simulated (AM1.5) solar illumination at 1 sun (100 mW/cm^2) in laboratory air. The device parameters are calculated using the equations [Eqn. 2.4-2.6].

2.8 Results and discussion

2.8.1 Growth mechanism of Au nanorods

The mechanism behind the seeded growth technique of Au nanorod formation can be explained in Eqs. 2.11 and 2.12.[41] In the growth solution as the mild reducing agent such as ascorbic acid is added, it will reduce the Ag$^+$ ions to Ag^0 atoms in the solution. But due to lower oxidation potential of Au^{3+} it starts oxidizing the Ag^0 atoms thus reducing itself to Au^0 atoms by the galvanic replacement. In growth solution each Au^{3+} ion oxidizes three Ag^0 atoms. Therefore, more the concentration of Ag$^+$ ions more will be the formation of Au^0 atoms. After reaching an optimum concentration, further increase in Ag$^+$ ion concentration cannot favour growth of Au nanorods. This is confirmed by the ultraviolet-visible spectra of Au nano dispersion. This may be attributed to the fact that the excess Ag$^+$ ions are adsorbed on the Au nanoparticle surface in the form of silver bromide (AgBr) and restrict the growth and stabilize the nanorods surface.[41]

$$Ag^+ + e^- \xrightarrow{\text{Ascorbic acid}} Ag^0 \qquad \text{Eqn. 2.11}$$

$$3Ag^0 + Au^{3+} \xrightarrow{\text{Galvanic replacement}} Au^0 + 3Ag^+ \qquad \text{Eqn. 2.12}$$

Since the seeded growth method is a kinetically controlled reaction having the seeds as the nucleation sites for nanoparticle growth, therefore growth of Au nanorods occurs with the addition of seeds. The surfactants form a soft template in which the size of the template varies with the surfactant concentration and the ionic strength of the solution. In the growth solution the surfactant capped seed becomes a part of the soft template and thus growth starts by diffusing the Au atoms into the template. It is seen that the addition of Ag$^+$ alters the chemistry at the interface of the growing particle and the growth solution. Addition of Ag$^+$ is very important for the synthesis of Au nanorods

because it allows for improved shape control and yield for short aspect ratio nanorods. In the growth process, the Ag^+ ions can first increase and then decrease the length of the nanorods. The decrease in the size at the highest concentration of Ag^+ ions may be due to the ionic strength effect.

2.8.2 Morphology (TEM, SEM and EDX)

A representative TEM image and selected area electron diffraction (SAED) pattern of
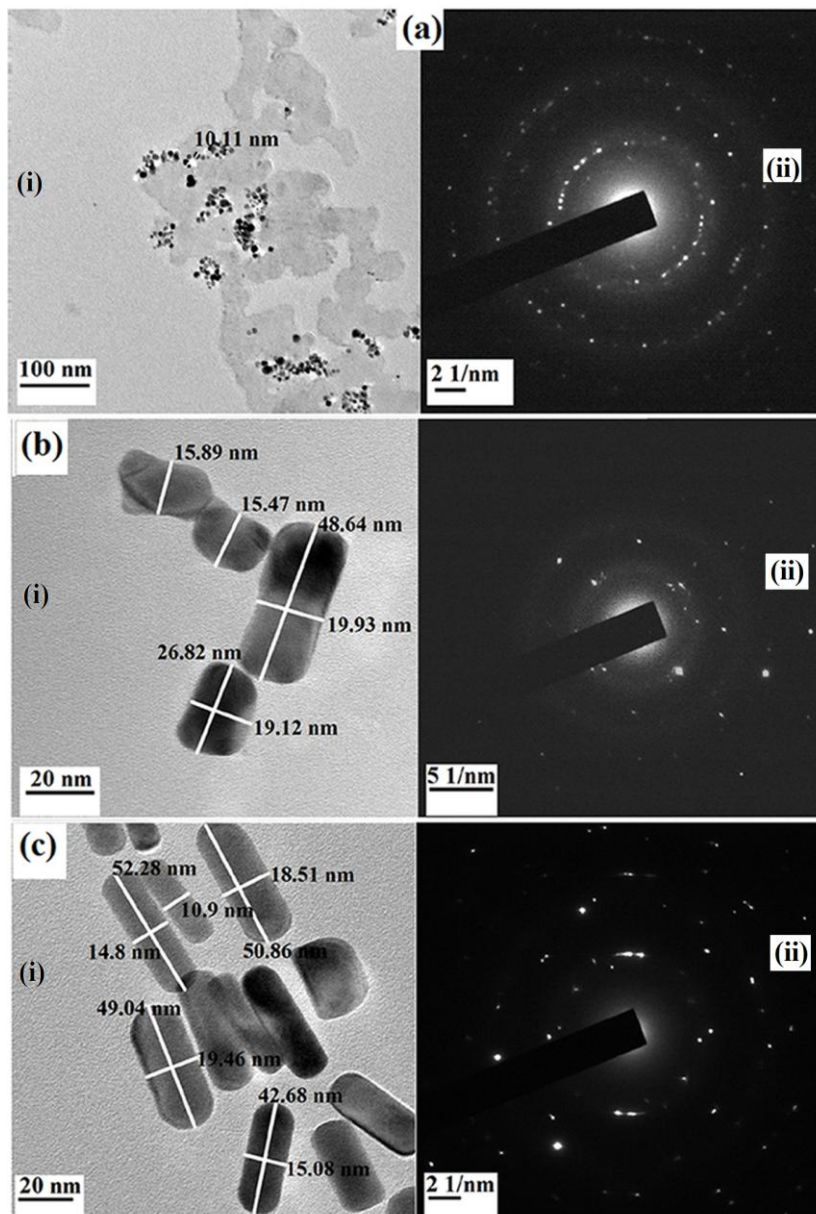
Fig. 2.10 (i) TEM image and (ii) SAED pattern of (a) Au seed solution, (b) Au nanorod (AR-2), (c) Au nanorods (AR-3.5). *AR- aspect ratio of the nanorods

Au seed and nanorods at 2.03 x 10^{-5} and 9.8 x 10^{-5} M Ag^+ ion concentrations is shown in Fig. 2.10a-c. The average particle diameter of the seeds is found to be 10 nm. TEM images of nanorods [Fig. 2.10b, c] show average diameter of particles is 15-17 nm. Fig. 2.10b shows nanoparticles prepared at 2.03 x 10^{-5} M Ag^+ ion concentration are of irregular shapes and growth of nanorods is incomplete with an aspect ratio of 2. TEM micrograph of the Au nanorods prepared at 9.8 x 10^{-5} M Ag^+ ion concentration [Fig. 2.10c] show well-defined nanoscaling, with highly mono-dispersed, capsule-shaped Au nanorods and a low polydispersity index. It is apparent that the size of the nanorods is less than 20 nm with an aspect ratio of 3.5. Corresponding SAED pattern confirms a good polycrystalline nature of nanorods.

Fig. 2.11 provides SEM micrograph and EDX spectrum of PVK/Au nanocomposite with Au nanorod (aspect ratio: 3.5). Morphological information about the surface and mixing of PVK/Au matrix is obtained by SEM analysis. SEM and EDX study shows a homogeneous mixing of the nanorods in the nanocomposites, which confirms the successful formation of the PVK/Au nanocomposites.
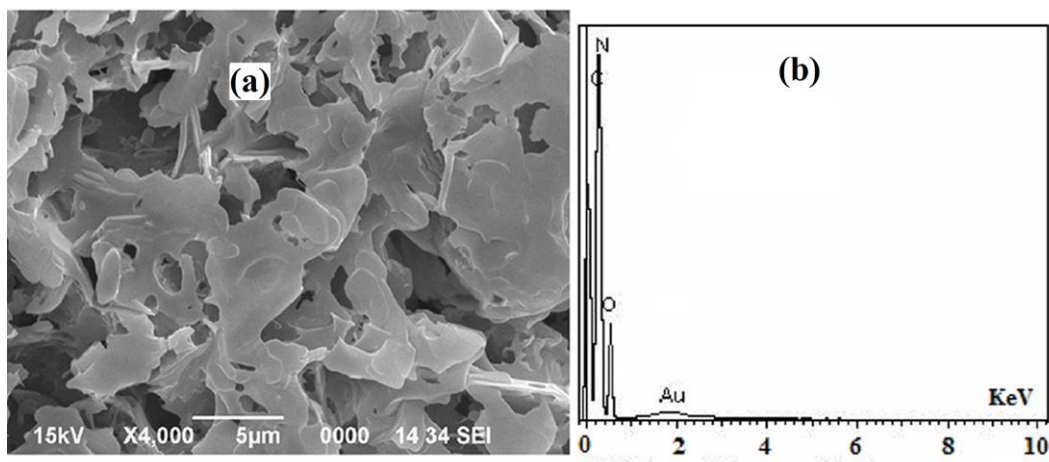

Fig. 2.11 (a) SEM image and (b) EDX spectrum of nanocomposite with Au nanorod (AR: 3.5). *AR- aspect ratio of the nanorods

2.8.3 Structural characteristics (FT-IR)

From FT-IR analysis [Fig. 2.12], various characteristic peaks are observed for PVK. The stretching frequency at 729 cm^{-1} is due to ring deformation of substituted aromatic structure. The band at 1015-1143 cm^{-1} is due to out-of plane deformation of vinylidene

group. The stretching frequencies at 1215-1322 cm^{-1} are due to C–N stretching, 1594 and 1444 cm^{-1} are due to aromatic C=C stretching. Stretching frequencies at 2930 and 3043 cm^{-1} are due to aliphatic C–H and aromatic C–H stretching respectively.[29] The absence of an absorption peak at 1600-1680 cm^{-1} is the indication of an effective polymerization at the vinyl group. These characteristic peaks are observed in all PVK/Au nanocomposites. A careful examination shows shifting in peak positions of the bands associated with C=C and C–N stretching towards higher wavenumber. This
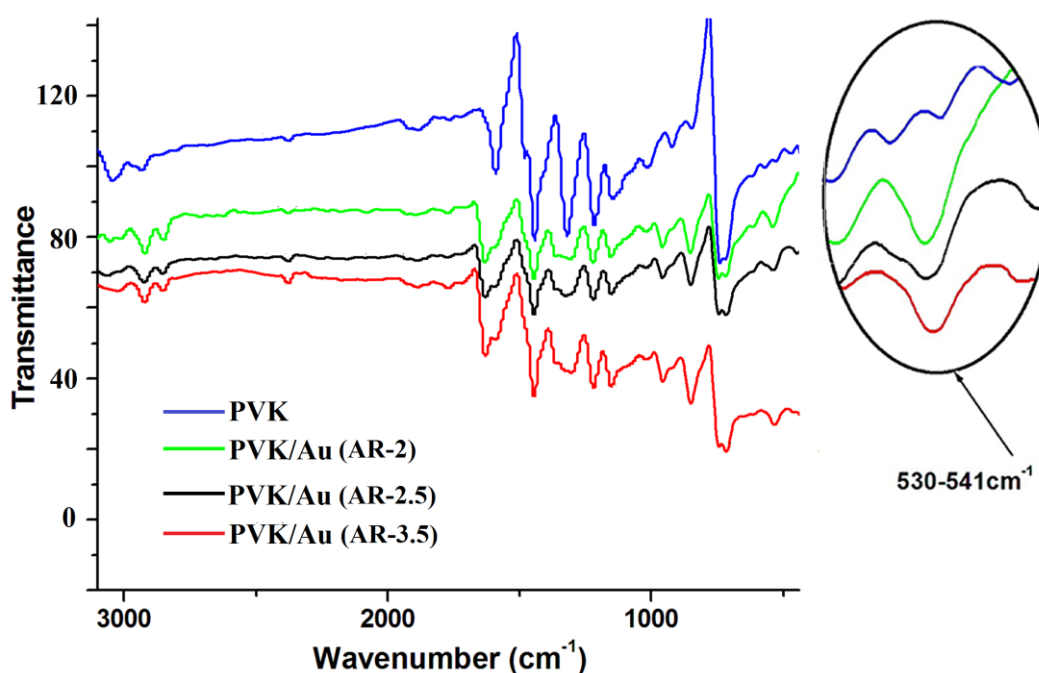
Fig. 2.12 FTIR spectra of polymer and nanocomposites with different aspect ratio (AR) of Au nanorods. Inset shows the absorption band of Au nanorods.

strongly attributes to the role of Au nanorods towards the modification of the electronic structure of the polymer due to which bonds become stronger in the nanocomposite compared to their virgin polymer. With increase in the aspect ratio of nanorods all the characteristic bands become more intense, which may be attributed to a strong interaction of high aspect ratio Au nanorods with the polymer backbone. Again, in the finger print region an absorption band is found at 530-541 cm^{-1} [Fig. 2.12 inset] in all PVK/Au nanocomposites, which is completely diminished in the virgin polymer. This band may arise due to the presence of Au nanorods in close proximity of nitrogen atom in PVK.

2.8.4 Optical analysis (UV-visible and PL)

Fig. 2.13a gives ultraviolet-visible spectra of Au seed solution and Au nanorods with different aspect ratio (2-3.5). Au seed solution gives an absorption maximum at around 522 nm which is due to surface plasmon resonance (SPR) of the spherical Au nanoparticles.[42] In contrast to the spherically symmetric Au nanoparticles, Au nanorods possess two different resonance modes at around 529 and 685 nm. These two separate modes arise due to electron oscillation across and along the long axis of the nanorods. These two modes are termed the transverse and longitudinal modes respectively.[41, 42] The aspect ratio of the nanorods has a significant influence on their longitudinal plasmon band. As we increase the Ag^+ ion concentration from 2.03 x 10^{-5} M to 9.8 x 10^{-5} M in the growth solution the transverse plasmon band shifts from 529 to 545 nm. This indicates that the aspect ratio of the nanorods increases with increase in Ag^+ ion concentration. But at a certain higher concentration of Ag^+ ion (13.3 x 10^{-5} M) the plasmon band shows a reverse trend (absorption maximum at 540 nm). This may be due to interaction of Ag^+ ion with the bromide ion of the structure directing agent (CTAB).[41] The Ag^+ ions are adsorbed at the Au nanoparticle surface in the form of AgBr that restrict the growth and stabilize the surface. Same trend is also observed in the case of longitudinal plasmon band.

With increase in Ag^+ ion concentration up to 9.8 x 10^{-5} M, the longitudinal plasmon band becomes more intense. But this peak gradually decreases with further increase in the Ag^+ ion concentration. This can also be explained by the interaction of Ag^+ ion with the bromide ion of CTAB. It is observed that the interactions between particles play a significant role in the optical response when the inter particle distance is comparable to or less than the particle size. When the Au nanoparticles near each other, they attract each other by dipole-dipole interactions. There may be two types of interactions. Due to the interaction of parallel collinear dipoles the plasmon wavelength shows a red-shift, while parallel but non-collinear dipoles produce blue-shift plasmon wavelengths. With increasing the Ag^+ ion concentration the absorption band becomes broader which may result from the overlapping of non-collinear dipole peak with the collinear dipole peak.[43, 44]

The UV-visible absorption spectra of PVK and its nanocomposites with Au nanorods were recorded in order to study the influence of nanorods on the optical properties of
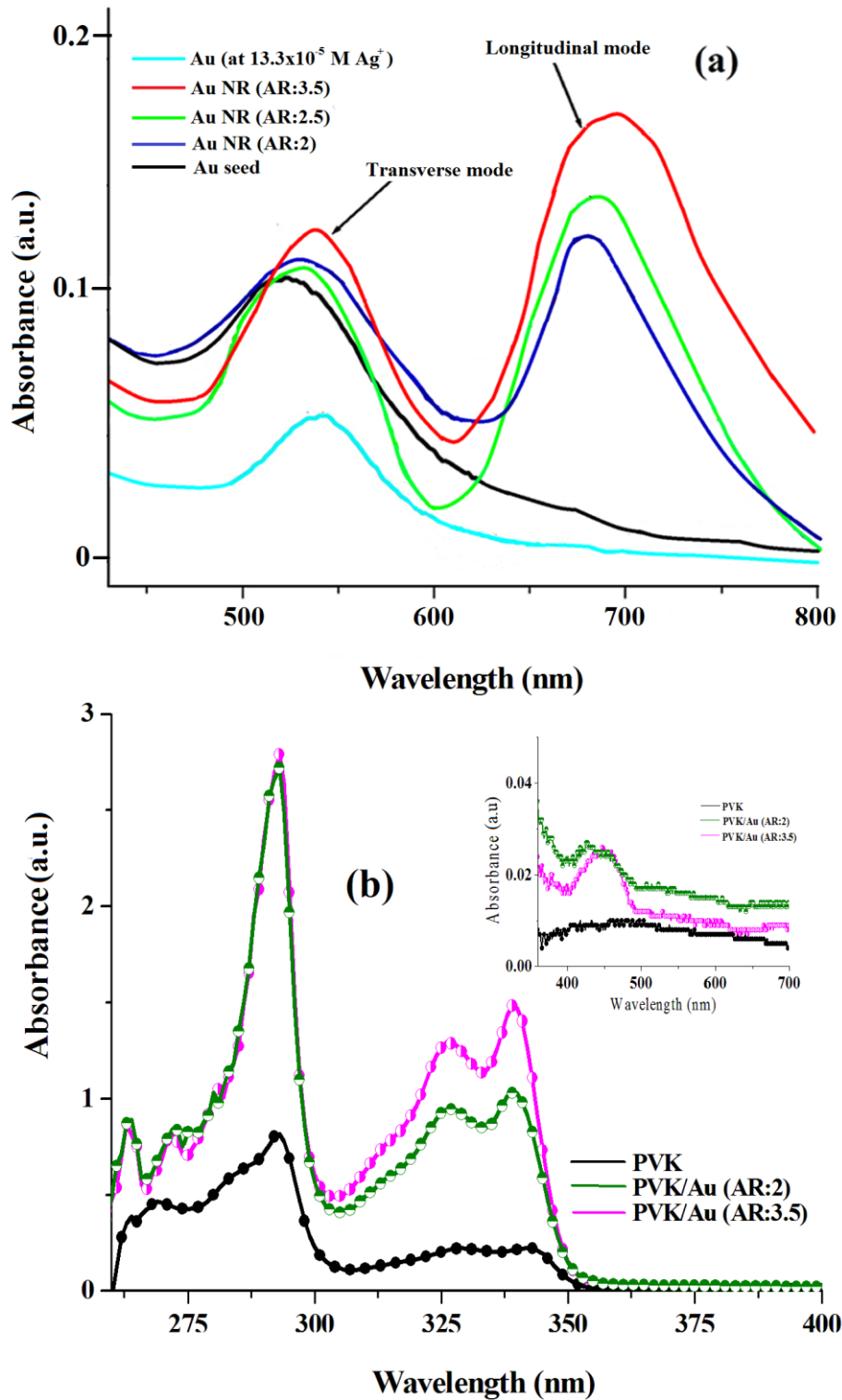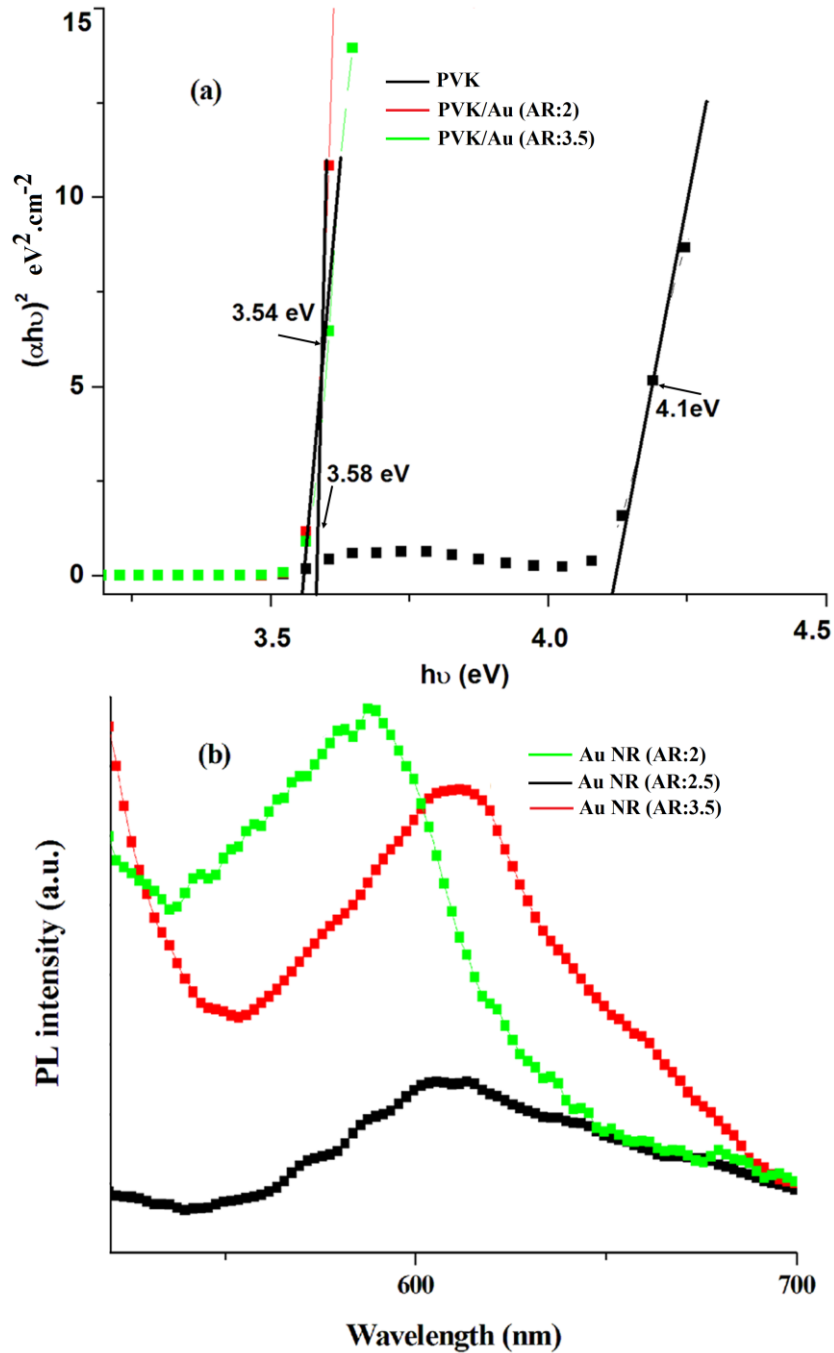
Fig. 2.13 (a) UV-visible spectra of Au nanorods and (b) spectra of polymer and nanocomposites with two different aspect ratio (AR) of Au nanorods. Inset shows absorption peak for Au nanorods in the nanocomposites. [*]*NR-nanorods*

PVK. Fig. 2.13b gives UV-visible spectra of PVK and PVK/Au nanocomposites. The

Fig. 2.14 (a) Optical band gap spectra of polymer and nanocomposites with two different aspect ratios (AR) of Au nanorods, (b) PL spectra of Au nanorods. *NR-nanorods,

optical absorption spectrum of PVK solution in THF shows intense peaks at 325 and 342 nm which are attributed to $\pi \to \pi^*$ electronic transition of the aromatic ring of the carbazole moieties.[32] The absorption peaks show a bathochromic shift to 338 and 352 nm in the nanocomposites which may be attributed to the fact that the incorporation of Au nanorods into the PVK matrix has an effect on the optical band gap of the polymer.

Au nanorods may be responsible for the formation of localized electronic states in the HOMO-LUMO gap of PVK. These localized electronic states can act as the trapping and recombination centers which enhances the low energy transitions. Consequently, a remarkable reduction in band gap is observed [Fig. 2.14a]. Thus, the incorporation of Au nanorods modifies the overall electronic structure of the polymer.[45] The band gap reduction has a linear relationship with the aspect ratio of nanorods. The overall optical absorbance of PVK is enhanced after the incorporation of Au nanorods and it is red-shifted remarkably by 240 nm in the nanocomposites. This may arise due to interaction between Au nanorods and polymer which results in combined effect in increasing absorption ability of the nanocomposites. The plasmon bands for Au nanorods are observed at 580 and 595 nm in PVK/Au nanocomposites in presence of Au nanorods of aspect ratio 2 and 3.5 respectively [Fig. 2.13 b inset] which were at 672 and 675 nm respectively for the corresponding Au nanorods. As a result of the incorporation of Au nanorods into the polymer matrix, agglomeration of nanoparticle is to some extent reduced that causes this hypsochromic shift.

Fig. 2.14b depicts photoluminescence (PL) spectra of different aspect ratio Au nanorods. Spectra were taken at an excitation wavelength of 510 nm. Due to the longitudinal plasmon resonance that absorbs at a longer wavelength the fluorescence intensity of Au nanorods is amplified and a large emission band is observed in the range 550-650 nm. The emission peak shifts towards higher wavelength as we increase the aspect ratio. With increase in the aspect ratio of nanorods, the luminescence quantum efficiency increases providing a red shift of the fluorescence maxima.[46] For Au nanorods of aspect ratio 2, the fluorescence peak is at 587 nm, which shows a bathochromic shift to 612 nm for nanorods of aspect ratio 3.5.

2.8.5 Study of electrochemical behaviour (CV)

Cyclic voltammetry (CV) is employed to investigate the redox behaviour of the polymer and the nanocomposites and to estimate their electrochemical band gap. CV peaks at positive potential are assigned to oxidation, whereas peaks at negative potential correspond to reduction. The HOMO and LUMO energy levels as well as the energy gap (E_g^{ec}) can be calculated from the onset oxidation potentials (ϕ_{ox}) and the

onset reduction potentials (ϕ_{red}) according to the previous equations [Eqn. 2.1-2.3]. Fig. 2.15 provide the CV curves of PVK and PVK/Au nanocomposite with two
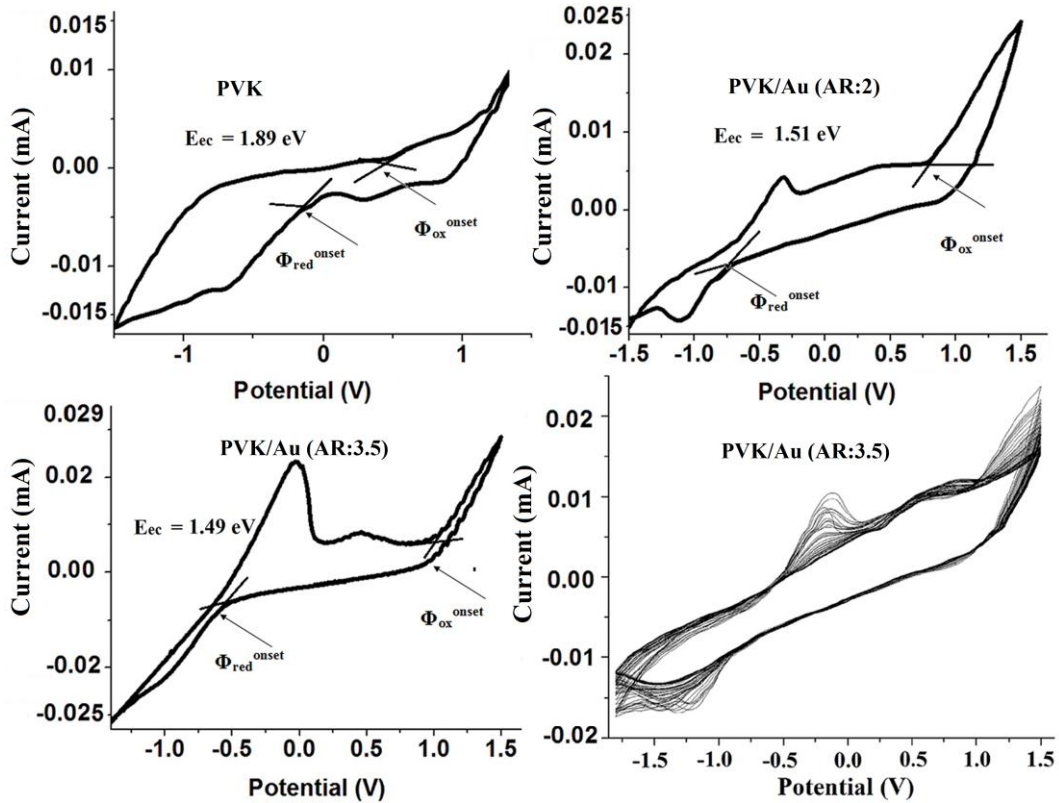
Fig. 2.15 Cyclic voltammetry curves of polymer and nanocomposites with two different aspect ratios (AR) of Au nanorods

different aspect ratio Au nanorods 2 and 3.5. It is observed that E_g^{ec} of PVK decreases linearly with increasing the aspect ratio of nanorods. For instance, E_g^{ec} decreases by 0.38 eV for nanorods of aspect ratio 2, whereas the same decreases by 0.4 eV for nanorods of aspect ratio 3.5 [Fig. 2.15]. These results can be correlated with the optical properties of the nanocomposites. Optical band gap of the polymer is reduced by 0.6 eV in the nanocomposites. This can be attributed to the role of Au nanorods on the modification of the electronic structure of PVK that causes enhancement of HOMO energy and diminution of LUMO energy which finally reduces the band gap of the polymer.[45] The nanocomposites show a very good electrochemical reversibility even after 50 repeated cycles [Fig. 2.15]. The CV study of PVK/Au nanocomposite up to 50th cycle reveals that cathodic and anodic peaks are nearly symmetrical above each other with minimum separation. The charge capacity remains almost unchanged after

few repeated cycles and it does not get diminished even after 50 repeated cycles. This property emphasizes that PVK/Au nanocomposite is very efficient material to be used in photovoltaic devices.

## 2.8.6 Study of photovoltaic performance

Photovoltaic properties of PVK/Au nanocomposites are studied by fabricating devices of the structure, ITO/PEDOT:PSS/PVK/Au nanocomposite:PCBM/Al. Here, the polymer acts as the donor material and Au nanorods act as a light absorber. The electron acceptor PCBM is mixed at a 1:1 ratio with the nanocomposite. With the absorption of light PVK produces electron–hole pair bound by strong coulomb interaction. This bound electron hole-pair; called exciton has a very little mobility and can easily recombine. For efficient electron transfer by exciton dissociation, an electron acceptor, PCBM is added. This causes a significant exciton separation and bound excitons migrate to the interface of BHJ, where they are dissociated due to the effect of the internal field. Thus, electrons are collected at the Al electrode through PCBM and holes are collected at the ITO via the electron blocking material, PEDOT:PSS layer, causing a voltage difference between the two electrodes. Fig. 2.16 shows the J-V curve of the hybrid BHJ photovoltaic device under AM 1.5 illumination at 100 mW/cm^2, and photovoltaic parameters, thus obtained from the J-V curve, are listed in Table 2.4. The device parameters are calculated using the equations [Eqn. 2.4-2.6].

Table 2.4 Summary of the photovoltaic performance of PVK/Au nanocomposite based hybrid photovoltaic devices

Photoactive layer	V_{oc} (V)	J_{sc} (mA/cm^2)	FF	PCE η (%)
PVK:PCBM	0.079	0.98	0.245	0.019
PVK/Au:PCBM (AR-2)	0.144	7.62	0.264	0.29
PVK/Au:PCBM (AR-2.5)	0.154	24.35	0.371	1.39
PVK/Au:PCBM (AR-3.5)	0.246	25.28	0.233	1.45

[*]AR-aspect ratio of the nanorods

Due to the anisotropy and transparency, metallic Au nanorod can be used as a good light absorber. They result in large degree of light harvesting in the BHJ
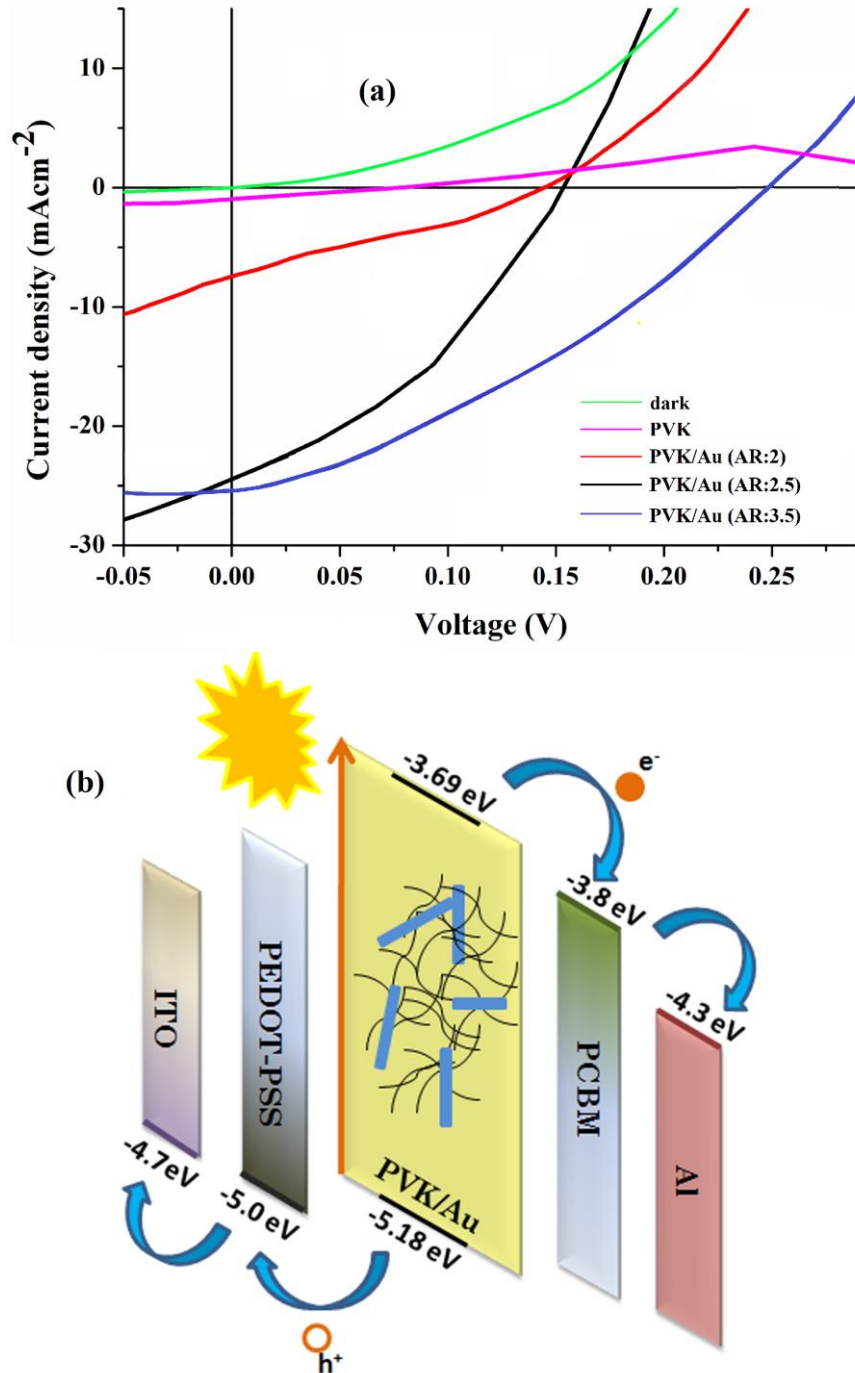
Fig. 2.16 (a) J-V curves of the fabricated devices under illumination, (b) Schematic energy-level diagram for the devices. *AR-aspect ratio

photovoltaic device through increased light trapping due to plasmonic effect that offers a high value of PCE.[47] The enhanced light absorption in the devices is significant from the absorption spectra of individual nanorods as well as nanocomposites [Fig. 2.13]. The absolute intensity increases with increase in aspect ratio, as shown in Fig. 2.13. The fabricated devices based on PVK/Au nanocomposites show an increased PCE

which linearly increases with increase in aspect ratio of the nanorods. The device without Au nanorods exhibits a PCE of only 0.02%, while for nanocomposite based devices efficiency becomes very high. For instance, the device with Au nanorods of aspect ratio 2 shows PCE of 0.29 %, while the same for Au nanorods of aspect ratio 3.5 is 1.45 %. A longer Au nanorod, gives rise to larger scattering intensity than the smaller one, resulting in prolonged light transport path, which further increases light absorption in the BHJ. Similarly, other photovoltaic parameters mainly J_{sc}, and V_{oc} are found to be higher for high aspect ratio nanorods. Shunt formation between two electrodes is hindered with increase in aspect ratio of nanorods that causes increase in V_{oc}.[34] Again, with increasing the aspect ratio more percolation pathways may form that facilitates the large transport of electrons and that is why, photocurrent density (J_{sc}) increases to a large extent.[34, 48]

2.9 Conclusion

By compiling the results, we have come to the following conclusion:

- ♦ We have demonstrated the seeded growth method of synthesis of various aspect ratio Au nanorods and the incorporation of nanorods into PVK matrix.
- ♦ The incorporation of high aspect ratio Au nanorods into PVK matrix reduces its electrochemical as well as optical band gap significantly by 0.4-0.6 eV.
- ♦ The PCE of a BHJ photovoltaic device can be increased from 0.29 % to a remarkable value (1.45 %) with the incorporation of high aspect ratio Au nanorods into the active layer.
- ♦ The incorporation of high aspect ratio nanorods results in large degree of light harvesting in the BHJ photovoltaic device compared to low aspect ratio nanorods. A longer Au nanorod, gives rise to larger scattering intensity than the smaller one, resulting in prolonged light transport path, which further increases light absorption in the BHJ.
- ♦ Shunt formation between two electrodes is hindered with increase in aspect ratio of nanorods that causes increase in V_{oc}. Again, with increasing the aspect ratio, more percolation pathways may form that facilitates the transport of electrons and that is why, J_{sc} increases to a large extent.

References

1. Grazulevicius, J.V., et al. *Prog. Polym. Sci.* **28**, 1297-1353, 2003.

2. Dridi, C., et al. *Nanotechnology* **19**, 375201-375211, 2008.

3. Hoegl, H. *Photoelectr. Eff. Polym.* **69**, 755-766, 1965.

4. Wang, G., et al. *Physica B: Condensed Matter* **279**, 116-119, 2000.

5. Tria, M.C., et al. *J. Mater. Chem.* **21**, 10261-10264, 2011.

6. Han, J., et al. *Macromol. Res.* **17**, 894-900, 2009.

7. Bhattacharyya, S., et al. *J. Phys. Chem. C* **114**, 11787-11795, 2010.

8. Bhattacharyya, S., & Patra, A. *Bull. Mater. Sci.* **35**, 719-725, 2012.

9. Daubler, T.K., et al. *Phys. Rev. B* **61**, 13515-13527, 2000.

10. Guo, F., et al. *Nat. Nanotechnol.* **7**, 798-802, 2012.

11. Wu, W., et al. *Chem. Phys. Lett.* **364**, 196-199, 2002.

12. Li, J., et al. *Solid State Electron.* **54**, 349-352, 2010.

13. Wu, W., et al. *Macromolecules* **36**, 6286-6288, 2003.

14. Wang, T.L., et al. *Macromol. Rapid Commun.* **30**, 1679-1683, 2009.

15. Kim, H.S., et al. *Synth. Met.* **117**, 289-291, 2001.

16. Kaune, G., et al. *Eur. Phys. J. E* **26**, 73-79, 2008.

17. Ling, J.Y., et al. *Chin. Sci. Bull.* **53**, 46-52, 2008.

18. Pokhrel, B., et al. *Mater. Manuf. Process.* **27**, 43-48, 2012.

19. Bayan, S., & Mohanta, D. *J. Electron. Mater.* **41**, 1955-1961, 2012.

20. Bayan, S., & Mohanta, D. *J. Appl. Phys.* **108**, 023512(1-6), 2010.

21. Jothi, N.S.N., et al. *Arch. Appl. Sci. Res.* **4**, 1698-1704, 2012.

22. Luo, Q.P., et al. *J. Mater. Chem.* **21**, 8709-8714, 2011.

23. Yan, L., & Liu, C.S. *T. Nonferr. Metal. Soc. China* **19**, 399-403, 2009.

24. Aneesh, P.M., et al. *Proc. SPIE* **6639**, 66390J (1-9), 2007.

25. Daniel, M.C., & Astruc, D. *Chem. Rev.* **104**, 293-346, 2004.

26. Al-Harbi, L.M., et al. *Mod. Appl. Sci.* **5**, 87-91, 2011.

27. Zhang, H., et al. *J. Phys. Chem. B* **108**, 3955-3958, 2004.

28. Mishra, S.K., et al. *Appl. Phys. A* **115**, 1193-1203, 2014.

29. Ghosh, D., & Biswas, M. *J. Polym. Res.* **16**, 245-254, 2009.

30. Viswanatha, R., et al. *Arch. Appl. Sci. Res.* **4**, 480-486, 2012.

31. Khalil, K.A., et al. *Mater. Sci. Appl.* **2**, 105-110, 2011.

32. Liu, G., et al. *J. Mater. Chem.* **21**, 6027-6033, 2011.

33. Abdullah, O.G., et al. *J. Mater. Sci. Mater. Electron.* **26**, 5303-5309, 2015.

34. Beek, W.J.E., et al. *J. Phys. Chem. B* **109**, 9505-9516, 2005.

35. Kong, F., et al. *Nanotechnology* **18**, 265707(1-5), 2007.

36. Mbhele, Z.H., et al. *Chem. Mater.* **15**, 5019-5024, 2003.

37. Gogoi, P., et al. *Prog. Org. Coat.* **77**, 87-93, 2014.

38. Gogoi, P., et al. *J. Appl. Polym. Sci.* **132**, 41490(1-9), 2015.

39. Patra, N., et al. *Compos. Part B Eng.* **43**, 3114-3119, 2012.

40. Mo, Z., et al. *J. Appl. Polym. Sci.* **112**, 573-578, 2009.

41. Nikoobakht, B., & El-Sayed, M.A. *Chem. Mater.* **15**, 1957-1962, 2003.

42. Delapierre, M.T., et al. *Gold. Bull.* **41**, 195-207, 2008.

43. Haynes, C.L., et al. *J. Phys. Chem. B* **107**, 7337-7342, 2003.

44. Chern, R.L., et al. *Phys. Rev. E* **76**, 016609(1-9), 2007.

45. Ghanipour, M., & Dorranian, D. *J. Nanomater.* **2013**, 1-10, 2013.

46. Mohamed, M.B., et al. *Chem. Phys. Lett.* **317**, 517-523, 2000.

47. Chen, S.F., et al. *Appl. Phys. Lett.* **104**, 213903(1-5), 2014.

48. Olson, D.C., et al. *J. Phys. Chem. C* **111**, 16640-16645, 2007.